

Mitochondrial fragmentation limits NK cell-based tumor immunosurveillance

Xiaohu Zheng^{1,2}, Yeben Qian³, Binqing Fu^{1,2}, Defeng Jiao^{1,2}, Yong Jiang³, Peng Chen³, Yiqing Shen^{1,2}, Huafeng Zhang¹, Rui Sun^{1,2}, Zhigang Tian^{1,2*} and Haiming Wei^{1,2*}

Natural killer (NK) cells have crucial roles in tumor surveillance. We found that tumor-infiltrating NK cells in human liver cancers had small, fragmented mitochondria in their cytoplasm, whereas liver NK cells outside tumors, as well as peripheral NK cells, had normal large, tubular mitochondria. This fragmentation was correlated with reduced cytotoxicity and NK cell loss, resulting in tumor evasion of NK cell-mediated surveillance, which predicted poor survival in patients with liver cancer. The hypoxic tumor microenvironment drove the sustained activation of mechanistic target of rapamycin-GTPase dynamin-related protein 1 (mTOR-Drp1) in NK cells, resulting in excessive mitochondrial fission into fragments. Inhibition of mitochondrial fragmentation improved mitochondrial metabolism, survival and the antitumor capacity of NK cells. These data reveal a mechanism of immune escape that might be targetable and could invigorate NK cell-based cancer treatments.

Natural killer (NK) cells are critical components in immunosurveillance against cancer^{1,2}. Deficiency or impaired activity of NK cells has been associated with an increased incidence rate and enhanced growth and metastasis in various types of cancers³. The early occurrence of natural immune surveillance leads to damage to transformed cells⁴, but as a tumor progresses, tumor cells escape immune detection.

Cellular metabolism is necessary for lymphocytes to survive, grow and function appropriately⁵. Studies of intratumoral T cell metabolism have revealed that tumor-imposed glucose restrictions mediate metabolic changes that lead to a loss of function⁶. Impaired glycolytic and oxidative metabolism restrains T cell effector functions during cancer^{7–9}. Some in vitro studies have revealed that NK cell survival is metabolically demanding and requires the presence of specific metabolic requirements after stimulation of receptors and cytokines^{10–14}. Additionally, mitophagy is essential for the antigen-specific formation of NK memory cells after infection¹⁵. There is growing recognition that inappropriate metabolic reprogramming underlies many aberrant disease microenvironments and that the manipulation of intracellular metabolism can temper or enhance immunity¹⁶. Thus, whether or not NK cells with abnormal metabolic reprogramming in the tumor microenvironment are a cause of immune escape is not clear.

Mitochondria are the central ‘hubs’ of metabolic signals¹⁷. Mitochondria are highly dynamic; their morphology is shaped continuously by fusion and fission reactions, and their intracellular distributions are altered¹⁸. Mitochondrial fusion drives the formation of linear or tubular networks and is important in sustaining mitochondrial respiration and cell survival. Additionally, mitochondrial fusion is needed to strengthen interactions with the endoplasmic reticulum, to enhance calcium flux^{19,20}. Fission of mitochondria into fragments accelerates reactive oxygen species (ROS) production, mediates apoptosis, maintains calcium homeostasis and induces mitophagy²¹. The function and metabolism of mitochondria are closely linked to their morphology²². Therefore, it is important to

maintain healthy mitochondrial morphology and networks by balancing the rates of fusion and fission. We aimed to ascertain whether inappropriate mitochondrial reprogramming is related to tumor-infiltrating NK (TINK) cell dysfunction.

Results

TINK cells from patients with liver cancer have fragmented mitochondria. We purified fresh TINK cells from patients with liver cancer, liver NK cells from patients with benign hemangioma/calculus and peripheral NK cells from normal donors for analyses of subcellular structure by transmission electron microscopy (TEM) (Supplementary Fig. 1a–c). We observed that the TINK cells mainly had small, fragmented, distinct mitochondria in the cytoplasm, whereas the liver NK cells and peripheral NK cells mainly had large, tubular, densely packed mitochondria (Fig. 1a,b). Both types of mitochondria were visible in all cells, but the frequencies in the distributions varied (Fig. 1a). Similar changes in the mitochondrial morphology of TINK cells were observed by confocal laser scanning microscopy (CLSM) (Fig. 1c,d and Supplementary Fig. 1d).

To initially assess the relationship between changes in mitochondrial morphology and NK cell function, we purified TINK cells and paired tumor-adjacent normal liver NK cells from patients with liver cancer, activated the cells with interleukin-12 (IL-12) and analyzed mitochondrial morphology and granzyme B expression. TEM revealed fragmented mitochondria and lower expression of granzyme B in the TINK cells relative to the liver NK cells (Fig. 1e,f). Statistical analyses showed a positive correlation between mitochondrial lengths and granzyme B levels (Fig. 1f). Furthermore, the TINK cells had a significantly lower mitochondrial mass (as measured by MitoTracker Green staining) than the paired tumor-adjacent normal liver NK cells (Fig. 1g). The mitochondrial membrane potential, which is an indicator of electron transport chain activity, was evaluated by staining with tetramethylrhodamine methyl ester (TMRM), was decreased significantly in the TINK cells (Fig. 1h).

¹Division of Molecular Medicine, Hefei National Laboratory for Physical Sciences at Microscale, The CAS Key Laboratory of Innate Immunity and Chronic Disease, School of Life Sciences, University of Science and Technology of China, Hefei, China. ²Institute of Immunology, University of Science and Technology of China, Hefei, China. ³Department of General Surgery, First Affiliated Hospital of Anhui Medical University, Hefei, China.

*e-mail: tzg@ustc.edu.cn; ustcwhm@ustc.edu.cn

We found that the TINK cells also had increased mitochondrial ROS levels (as measured by MitoSOX) (Fig. 1i).

Human NK cells can be classified into two main classic subsets: CD56^{bright}CD16⁻ and CD56^{dim}CD16⁺. To assess whether the different subsets of NK cells exhibit variation in mitochondrial morphology, we purified the two subsets of peripheral NK cells for TEM analyses of subcellular structure. We found that the two subsets of cells had similar mitochondrial morphology (Supplementary Fig. 1e). We also purified tumor-infiltrating T cells for TEM analyses of mitochondrial morphology and found that both small fragmented and large tubular mitochondria were present in the cytoplasm (Supplementary Fig. 1f). Both types of mitochondria were visible in all cells, and the frequency of distribution was not altered between the tumor-infiltrating T cells and normal liver T cells (Supplementary Fig. 1f).

Next, we assessed changes in mitochondrial morphology and the state of TINK cells at the transcriptomic level. We purified fresh TINK cells from patients with liver cancer, NK cells from the junction of tumor and normal liver tissue (tumor-edge NK cells) in patients with liver cancer, peripheral NK cells from patients with liver cancer, liver NK cells from patients with benign hemangioma or calculus and peripheral NK cells from donors with no diagnosed disease (normal peripheral NK cells), and determined relative gene expression (Supplementary Fig. 1a). The transcriptional profiles of the TINK cells were similar to those of the tumor-edge NK cells but were different from those of the liver NK cells and normal peripheral NK cells (Fig. 1j). Gene Ontology enrichment analysis revealed altered metabolism, including reprogrammed mitochondrial metabolic processes involved in mitochondrial morphogenesis and ROS metabolic processes, to be a hallmark of the TINK cells (Fig. 1k). Furthermore, the TINK cells upregulated the expression of numerous mitochondrial fission-related genes, such as *INF2*, *MIEF2*, *FIS1* and *GDAP1* (Fig. 1l). High expression of fission genes has been shown to drive mitochondria into discrete fragments²³.

Taken together, these results revealed entirely different mitochondrial structures in human NK cells from a pathological tumor microenvironment and physiological organ systems. Specifically, TINK cells mainly had fragmented mitochondria that were different from the mitochondria in liver NK cells and peripheral NK cells.

A hypoxic microenvironment induces mitochondrial fragmentation in NK cells. To explore the cause of mitochondrial fragmentation in TINK cells, we assessed the transcriptional profiles of TINK cells and liver NK cells. We found that the genes showing increased expression in the TINK cells were enriched for signatures of hypoxia, such as *HK2*, *SLC7A5*, *SLC2A3* and *KDM3A* (Fig. 2a,b).

Hypoxia is a key feature of the tumor microenvironment²⁴. We employed hypoxia-inducible gene signatures and a surrogate marker—glucose transporter 1 (ref. ²⁵)—as estimates of the hypoxic state in samples from The Cancer Genome Atlas (TCGA) hepatocellular carcinoma (HCC) dataset. We identified enhanced hypoxic states in the HCC tissue samples relative to the normal liver tissue samples (Fig. 2c and Supplementary Fig. 2a). Indeed, unsupervised clustering analyses of the hypoxic signatures divided the patients with HCC into two subsets: severe hypoxia ($n=95/365$) and mild hypoxia ($n=270/365$) (Supplementary Fig. 2a).

We then sought to ascertain whether a hypoxic environment induces mitochondrial fragmentation in NK cells. We cultured purified normal peripheral NK cells and liver NK cells under hypoxic (<1% O₂) or normoxic (20% O₂) conditions for 3–7 d. TEM and CLSM revealed that hypoxic stress led to significant mitochondrial fragmentation (Fig. 2d–g and Supplementary Fig. 3a–e). We also carried out mitochondrial dynamic imaging of live hypoxic and normal human NK cells during 120 min of filming by time-lapse microscopy. NK cells had increased mitochondrial division under hypoxia (Supplementary Videos 1–3 (hypoxic NK), Supplementary Videos 4–6 (normal NK) and Supplementary Fig. 3f,g). Hypoxic stress also induced reductions in mitochondrial mass and mitochondrial membrane potential (Fig. 2h,i). NK cells cultured under hypoxia showed reduced expression of granzyme B, interferon- γ (IFN- γ) and CD107a after activation, suggesting impaired functionality (Fig. 2j–l). Immunoblot analyses suggested that the expression of the mitophagy-related proteins PINK1 and LC3B was not significantly increased during hypoxic culture for 3 d (Supplementary Fig. 3h).

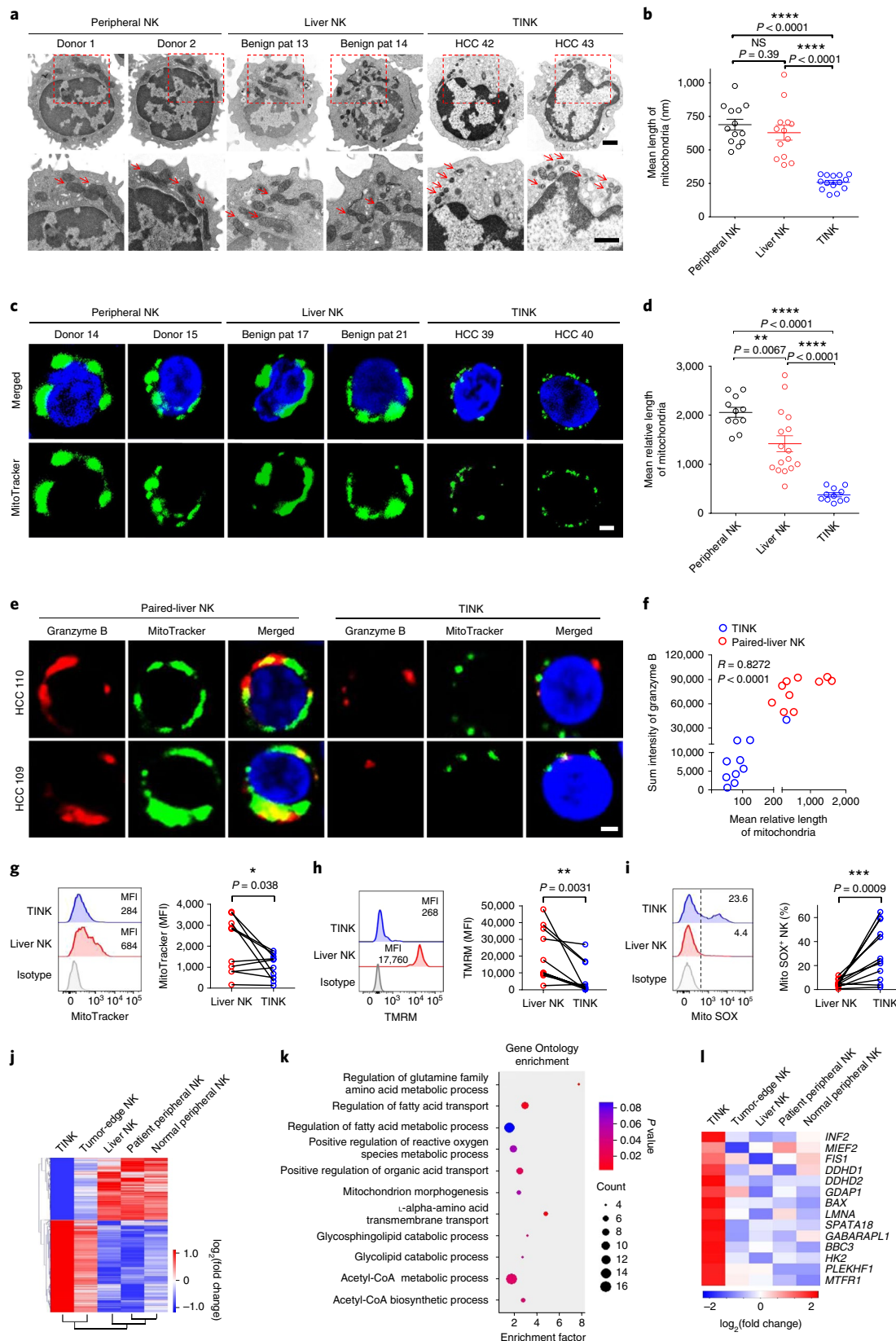
To directly assess the contribution of the hypoxic microenvironment on mitochondrial fragmentation in TINK cells, we purified TINK cells cultured under hypoxic or normoxic conditions and analyzed mitochondrial morphology. We found that freshly isolated and hypoxia-cultured TINK cells mainly had small fragmented mitochondria, while normoxic culture promoted the formation of large agminated mitochondria in TINK cells (Fig. 2m,n).

Next, we assessed the influence of hypoxia on mitochondrial structure in NK cells at the transcriptomic level. We cultured purified normal peripheral NK cells under hypoxic or normoxic conditions to determine gene expression. We found that the hypoxia-stressed NK cells were different from the normoxic-cultured NK cells (Fig. 2o and Supplementary Fig. 3i). The hypoxia-stressed NK cells upregulated the expression of numerous mitochondrial fission-related genes (Fig. 2p). Taken together, these results showed that hypoxic stress promoted mitochondrial fragmentation in NK cells.

Fig. 1 | Mitochondrial fragmentation in TINK cells. **a**, TEM showing the mitochondrial morphology of purified NK cells. The bottom row of images are magnified views of the areas indicated by red dashed boxes above. Pat, patient. Red arrows denote mitochondria. **b**, Mitochondrial length, as analyzed by TEM in $n=13$ patients with liver cancer, $n=13$ patients with benign hemangioma/calculus and $n=14$ donors with no diagnosed disease. Each dot represents the mean length of the mitochondria in a sample. **c**, CLSM images showing purified NK cells in which the mitochondria (MitoTracker; green) and nucleus (Hoechst; blue) are stained. **d**, Relative lengths of the mitochondria, as analyzed by CLSM in $n=11$ patients with liver cancer, $n=16$ patients with benign hemangioma/calculus and $n=11$ donors with no diagnosed disease. The images were digitized using IMARIS software. Each dot represents the mean relative length of the mitochondria in a sample. **e**, Purified TINK cells and paired tumor-adjacent normal liver NK cells activated with IL-12 were assessed by CLSM (MitoTracker, green; granzyme B, red; Hoechst, blue). **f**, Each dot represents the mean relative mitochondrial length per patient correlated with the mean intensity of granzyme B staining. The Spearman correlation coefficient (R) and P value are shown ($n=10$ patients with liver cancer). **g–i**, Left: live CD45⁺CD56⁺CD3⁻ TINK cells and paired tumor-adjacent normal liver NK cells were stained with MitoTracker Green (**g**), TMRM (**h**) or MitoSOX (**i**) and analyzed by flow cytometry. Right: the relative mean fluorescence intensities (MFIs) of $n=10$ patients (**g**) and $n=11$ patients (**h**) are shown, along with the proportion of MitoSOX⁺ NK cells in $n=12$ patients (**i**). In **g–i**, the isotype represents the negative control. **j–l**, The gene expression of purified TINK, tumor-edge NK, patient peripheral NK, liver NK and normal peripheral NK cells is shown. **j**, The 3,438 genes with differential expression (greater than twofold) in TINK cells compared with tumor-edge NK cells, liver NK cells, patient peripheral NK cells and normal peripheral NK cells were selected for heat map analysis. Each column depicts the mean of $n=2$ samples. In total, $n=10$ samples are shown. **k**, A Gene Ontology enrichment analysis of the differentially expressed genes was performed to evaluate enriched biological processes. The enrichment of metabolism-related biological processes is shown. **l**, Heat map showing the normalized expression of mitochondrial fission-related genes. All data represent means \pm s.d. Data were analyzed by two-way ANOVA (**b** and **d**) or two-tailed paired Student's t -test (**g–i**). * $P < 0.05$; ** $P < 0.01$; *** $P < 0.005$; **** $P < 0.0001$. Scale bars, 1 μ m.

Mechanistic target of rapamycin-GTPase dynamin-related protein 1 (mTOR-Drp1) activity in NK cells in a hypoxic tumor microenvironment causes mitochondrial fragmentation. Mitochondria are highly dynamic, and their architecture is shaped by opposing fusion and fission reactions¹⁸. Drp1 is the main regulator

of mitochondrial fission, and it drives division at specific points along mitochondria²⁶. Here, we found that, compared with paired tumor-adjacent normal liver NK cells, TINK cells upregulated the pro-fission activity of Drp1 by phosphorylation of Drp1 at Ser616 (Fig. 3a). Studies have shown that activated Drp1^{Ser616} proteins are



recruited to the mitochondrial membrane to form multimeric spirals that constrict and 'pinch' the mitochondrion apart^{18,27}. CLSM revealed an abundance of the Drp1^{ser616} protein localized in the cytoplasm of TINK cells but not in that of normal liver NK cells (Fig. 3b). The co-localization of fragmented mitochondria and Drp1^{ser616} is shown in Fig. 3b. Hypoxic stress also promoted Drp1 phosphorylation at its activating site, Ser616, but not at its suppressive site, Ser637 (Fig. 3c). Consistent with TINK cells, hypoxic-cultured liver NK cells and peripheral NK cells showed significant assembly of Drp1^{ser616} proteins in the cytoplasm (Fig. 3d and Supplementary Fig. 4a). We investigated whether excessive fission causes mitochondrial fragmentation in a manner dependent on Drp1 expression in TINK cells. Using a genetic approach to knockdown Drp1 expression in TINK cells, we noted the recovery of mitochondrial morphology in TINK cells after knocking down Drp1 expression (Fig. 3e). We also treated purified TINK cells with two widely used small-molecule inhibitors of mitochondrial fission: mdivi-1 and dynasore (Dyn)^{28,29}. We found that these two inhibitors could promote the formation of large, tubular, agminated mitochondria in TINK cells (Fig. 3f and Supplementary Fig. 4b). Knocking down Drp1 expression and treating cells with mdivi-1 and Dyn enabled the mitochondrial morphology of hypoxic-cultured NK cells to recover to a state similar to that of normal NK cells (Supplementary Fig. 4c,d). Mitochondrial fission process 1 can also control mitochondrial fission. We found that hypoxia could not significantly promote the expression of mitochondrial fission process 1 (Supplementary Fig. 4e). We wanted to exclude the possibility of an impaired fusion event leading to mitochondrial fragmentation in TINK cells. Therefore, we analyzed a range of known regulators of fusion activity, including mitofusin-1 (Mfn-1), Mfn-2, Mfn-G and optic atrophy protein 1, at the gene and protein levels^{30,31}. We found no changes in the gene or protein expression of these molecules in TINK cells or hypoxia-stimulated NK cells relative to their respective controls (Fig. 3c and Supplementary Fig. 4f).

Next, we wanted to investigate how hypoxia enhances Drp1 phosphorylation at the Ser616 site. Studies have shown that hypoxia-inducible transcription factor-1 α is required for cellular adaptation to low oxygen levels in non-immune cells³². We measured hypoxia-inducible transcription factor-1 α levels in TINK cells and their respective controls, but found no differences among these groups of NK cells (Supplementary Fig. 4g,h). However, enrichment analyses of the transcriptional profiles of TINK cells and liver NK cells revealed that the TINK cells had enriched mTOR signaling (Fig. 3g). Using flow cytometry, we found that the two subsets of

NK cells (CD56^{bright}CD16⁻ and CD56^{dim}CD16⁺ cells) in tumor tissue had a higher mTOR signature (phospho-S6 ribosomal protein (P-S6)) than the subsets of paired tumor-adjacent normal liver NK cells (Fig. 3h). Hypoxic stress aggravated the phosphorylation of the S6 ribosomal protein and mTOR^{S2448} (Fig. 3i). Treatment with the mTOR inhibitor rapamycin inhibited hypoxia-induced mitochondrial fragmentation in NK cells (Fig. 3j). Furthermore, mTOR inhibition reduced phospho-Drp1^{ser616} levels, as evidenced by immunoblotting and CLSM (Fig. 3k,l). We wished to explore how hypoxia leads to mTOR activation. Enrichment analyses of the transcriptional profiles of hypoxia-stressed NK cells and normoxic-cultured NK cells revealed that hypoxic NK cells had enriched AKT signaling (Supplementary Fig. 4i). We verified that hypoxia upregulated the phosphorylation (Ser473) of AKT in NK cells (Supplementary Fig. 4j,k). Treatment with an AKT inhibitor inhibited hypoxia-induced mTOR activation in NK cells (Supplementary Fig. 4l). These results showed that hypoxia-induced mTOR activation was dependent on AKT signaling.

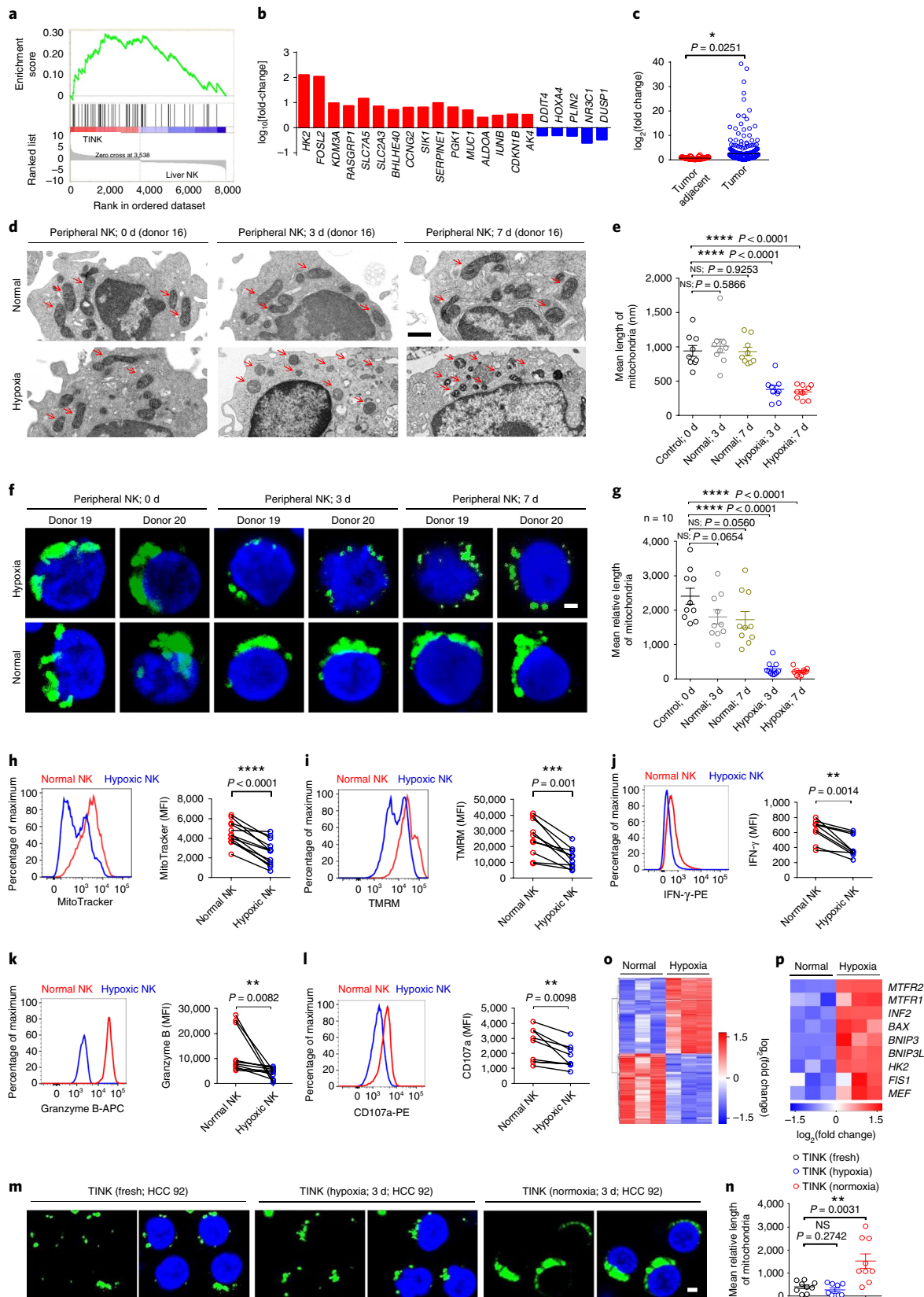
Taken together, these results showed that hypoxia induced excessive fission, which caused mitochondrial fragmentation that was dependent on increased mTOR-Drp1 signaling in NK cells.

Mitochondrial fragmentation affects NK cell survival in the tumor microenvironment. We explored whether mitochondrial fragmentation is correlated with a deficiency in the antitumor effects of NK cells that leads to tumor progression. Mitochondrial fragmentation is known to promote the production of ROS and the release of cytochrome *c*; downstream caspase activation is the main intrinsic pathway of apoptosis²¹. During hypoxic culture, we found that NK cells showed increased levels of the apoptosis-related protein cleaved caspase 3 in the later phase (7 d) but not in the early phase (3 d), which suggested that apoptosis occurred after mitochondrial fragmentation (Supplementary Fig. 5a). We also observed that the genes with increased expression in TINK cells were enriched for apoptosis signatures (Fig. 4a). Flow cytometry showed that two subsets of TINK cells (CD56^{bright}CD16⁻ and CD56^{dim}CD16⁺ cells) showed higher levels of apoptosis than the same two subsets in normal liver NK cells (Fig. 4b). Furthermore, hypoxia-stimulated phospho-mTOR^{high} NK cells showed enhanced expression of cleaved caspase 3 (Supplementary Fig. 5b). Analyses of NK cell numbers in patients with liver cancer showed reductions in the total number of NK cells and the numbers of the two main subsets of NK cells (CD56^{bright}CD16⁻ and CD56^{dim}CD16⁺ cells) in the tumor microenvironment (Fig. 4c and Supplementary Fig. 5c,d).

Fig. 2 | Hypoxia induces mitochondrial fragmentation in NK cells. **a**, Gene set enrichment analysis (GSEA) revealed an increase in hypoxic signatures (enrichment plot: LEONARD_HYPOXIA, M19622; Supplementary Table 4) in TINK cells compared with normal liver NK cells. GSEA plots are shown. **b**, Fold-changes in hypoxia-related genes in TINK cells compared with liver NK cells. In **a** and **b**, data are from gene expression profiling analyses and are representative of $n = 4$ patients. **c**, RNA sequencing was used to analyze the level of a hypoxic marker (glucose transporter 1) in tumor ($n = 374$) and tumor-adjacent normal liver samples ($n = 50$). Data are from the TCGA HCC dataset. **d,f**, TEM (**d**) and CLSM (MitoTracker, green; Hoechst, blue) images (**f**) showing the mitochondrial morphology in purified peripheral NK cells. NK cells were cultured under hypoxic ($O_2 < 1\%$) or normoxic conditions for 3–7 d. Red arrows in **d** denote mitochondria. **e**, The lengths of the mitochondria in $n = 9$ donors were analyzed by TEM. Each dot represents the mean length of the mitochondria in one donor. **g**, The relative lengths of the mitochondria in $n = 10$ donors were analyzed by CLSM (the images were digitized using IMARIS software). Each dot represents the mean relative length of a sample. **h,i**, Left: the mitochondrial mass (MitoTracker Green staining; **h**) and mitochondrial membrane potential (TMRM staining; **i**) of hypoxic- and normoxic-cultured peripheral NK cells (gate: live CD45⁺CD56⁺CD3⁻) were analyzed by flow cytometry. The results are representative of $n = 12$ (**h**) and $n = 10$ donors (**i**). **j–l**, Flow cytometry was used to evaluate the expression of IFN- γ (**j**), granzyme B (**k**) and CD107a (**l**) in hypoxic- and normoxic-cultured peripheral NK cells from $n = 9$ (**j** and **l**) or $n = 10$ donors (**k**) activated with IL-12 (**j** and **k**) or tumor cell co-culture (**l**). **h–l**, Left: representative MFI plot of a sample. Right: statistical calculation of all samples. **m**, CLSM images showing the mitochondrial morphology in purified TINK cells. TINK cells were generated from freshly isolated cells or cultured under hypoxic ($O_2 < 1\%$) or normoxic conditions for 3 d (MitoTracker, green; Hoechst, blue). **n**, The relative lengths of the mitochondria in $n = 9$ patients were analyzed by CLSM. **o,p**, Gene expression of hypoxic- and normoxic-cultured peripheral NK cells ($n = 3$ human samples in each group). **o**, In total, 1,069 differentially expressed genes (greater than twofold) were selected for heat map analyses. **p**, Heat map of the genes related to mitochondrial fission. Data were analyzed by two-tailed paired Student's *t*-test (**c** and **h–l**) or ANOVA (**e**, **g** and **n**). * $P < 0.05$; ** $P < 0.01$; *** $P < 0.005$; **** $P < 0.0001$. Data represent means \pm s.d. Scale bars, 1 μ m.

CD49a has been reported as an important marker for the division of liver NK cell subsets in mice³³. In the present study, we found a small population of CD49a⁺ NK cells in normal liver tissue (Fig. 4c and Supplementary Fig. 5c,d). In the tumor microenvironment, some CD16⁻ NK cells were CD49a⁺ (Supplementary

Fig. 5c,d), and the CD49a⁺ NK cells had an NKp46⁺CD127⁻CD16⁻Tbet⁺Eomes⁺CD103⁺CD69⁺ phenotype similar to the phenotype of human liver-resident NK cells³⁴ (Supplementary Fig. 5e,f). In addition, TINK cells showed different phenotypes compared with paired tumor-adjacent normal liver NK cells. For example, TINK



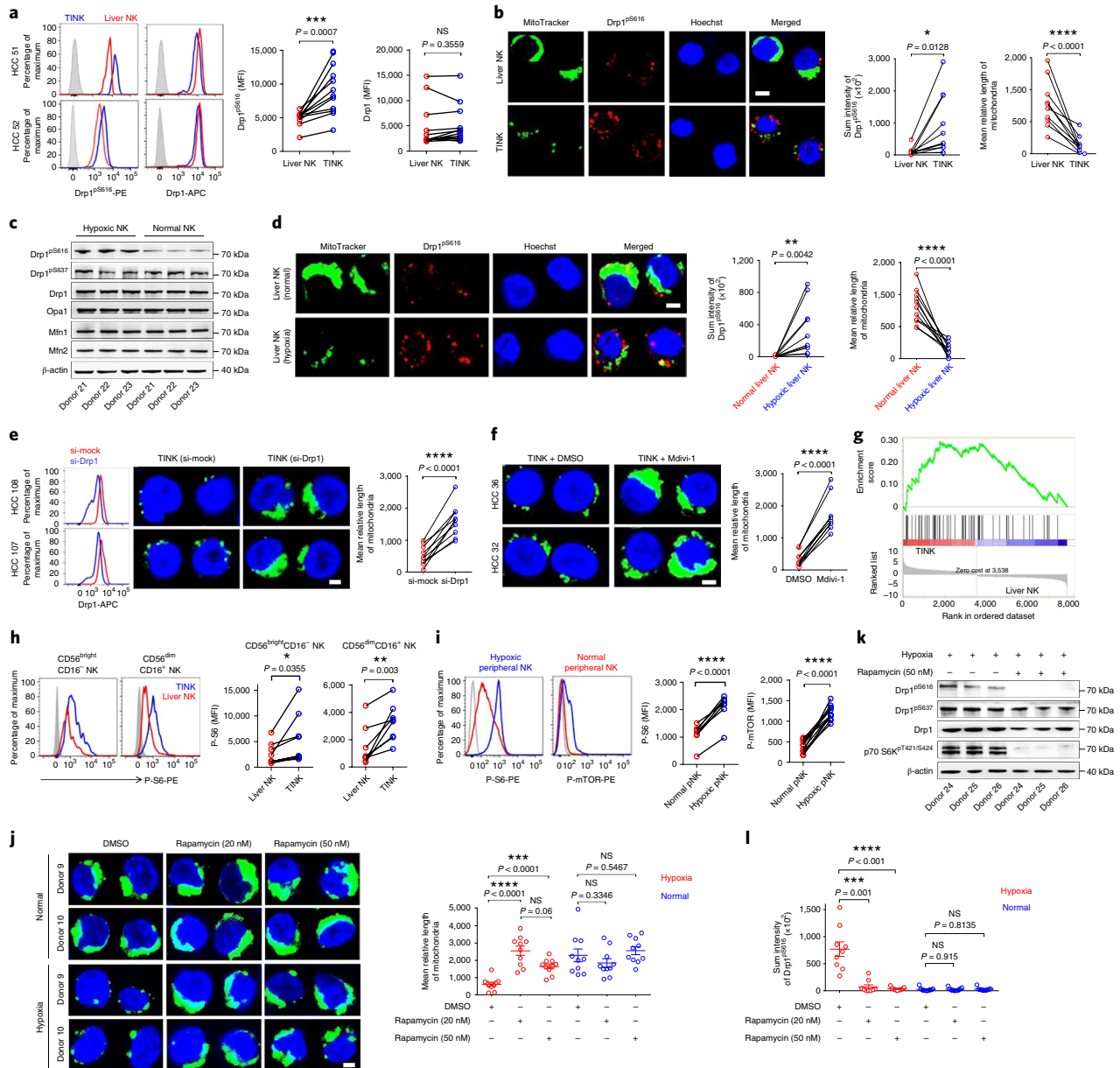


Fig. 3 | Hypoxia causes mitochondrial fragmentation by enhancing the constitutive activation of mTOR-Drp1 signaling. **a**, Flow cytometry was used to analyze the expression of Drp1 and Drp1 phosphorylated at Ser616 (Drp1^{pS616}) in TINK cells and paired tumor-adjacent normal liver NK cells (gate: 7-AAD⁻CD45⁺CD56⁺CD3⁻) in $n=12$ patients. Left: representative MFI plot of a sample. Right: statistical calculation of all samples. **b**, Left: purified TINK cells and paired tumor-adjacent normal liver NK cells were evaluated by CLSM. The co-localization of mitochondria and Drp1^{pS616} is shown. The mean intensity of Drp1^{pS616} staining (middle) and relative lengths of mitochondria (right) in $n=11$ patients were analyzed by CLSM (green, MitoTracker; red, Drp1^{pS616}; blue, Hoechst). **c**, Immunoblotting was used to analyze cell protein extracts from purified peripheral NK cells. NK cells were cultured under hypoxic ($O_2 < 1\%$) or normoxic conditions for 3 d. Data are representative of $n=2$ experiments and $n=6$ donors. **d**, Left: CLSM images show the co-localization of mitochondria and Drp1^{pS616} in purified liver NK cells. NK cells were cultured under hypoxic or normoxic conditions ($n=10$ patients). As in **b**, the mean intensity of Drp1^{pS616} staining (middle) and relative lengths of mitochondria (right) were analyzed. **e, f**, CLSM images (middle in **e**; left in **f**) show the recovery of mitochondrial morphology in purified TINK cells after knocking down Drp1 expression (si-Drp1) (**e**; $n=10$ patients) and treating the cells with mdivi-1 (10 nM) (**f**; $n=9$ patients). Left (**e, f**): representative knockdown efficiency plots are shown. Right (**e, f**): Statistical calculation of all samples. **g**, GSEA showing the enrichment of mTOR1 signaling (enrichment plot: HALLMARK MTORC1 SIGNALING; Supplementary Table 4) in TINK cells compared with normal liver NK cells. Data are representative of $n=4$ patients. **h**, Flow cytometry was used to analyze the phosphorylation of S6 (P-S6) in NK cells in tumors and paired tumor-adjacent normal liver ($n=8$ patients). **i**, Flow cytometry was used to analyze the expression of P-S6 and the phosphorylation of mTOR^{S2448} (P-mTOR) in hypoxic- and normoxic-cultured peripheral NK cells from $n=7$ (P-S6) and $n=12$ donors (P-mTOR). **h, i**, Left: representative MFI plot of a sample. Middle and right: statistical calculation of all samples. **j**, Left: CLSM images showing the recovery of mitochondrial morphology in hypoxic-cultured peripheral NK cells from $n=10$ donors after treatment with rapamycin. Right: mean relative lengths of mitochondria (one data point per patient). **k**, Immunoblotting was used to analyze cell protein extracts from hypoxic-cultured peripheral NK cells after treatment with rapamycin or DMSO. Data are representative of $n=2$ experiments and $n=6$ donors. **l**, Intensity of Drp1^{pS616} expression in hypoxic- and normoxic-cultured peripheral NK cells after treatment with rapamycin or DMSO (solvent control), as analyzed by immunofluorescence ($n=9$ donors). **a, h, i**, Grey plots are representative of antibody isotype control. Data were analyzed by two-tailed paired Student's *t*-test (**a, b, d-f, h, i**) or two-way ANOVA (**j, l**). * $P < 0.05$; ** $P < 0.01$; *** $P < 0.005$; **** $P < 0.0001$. Data represent means \pm s.d. Scale bars, 1 μ m.

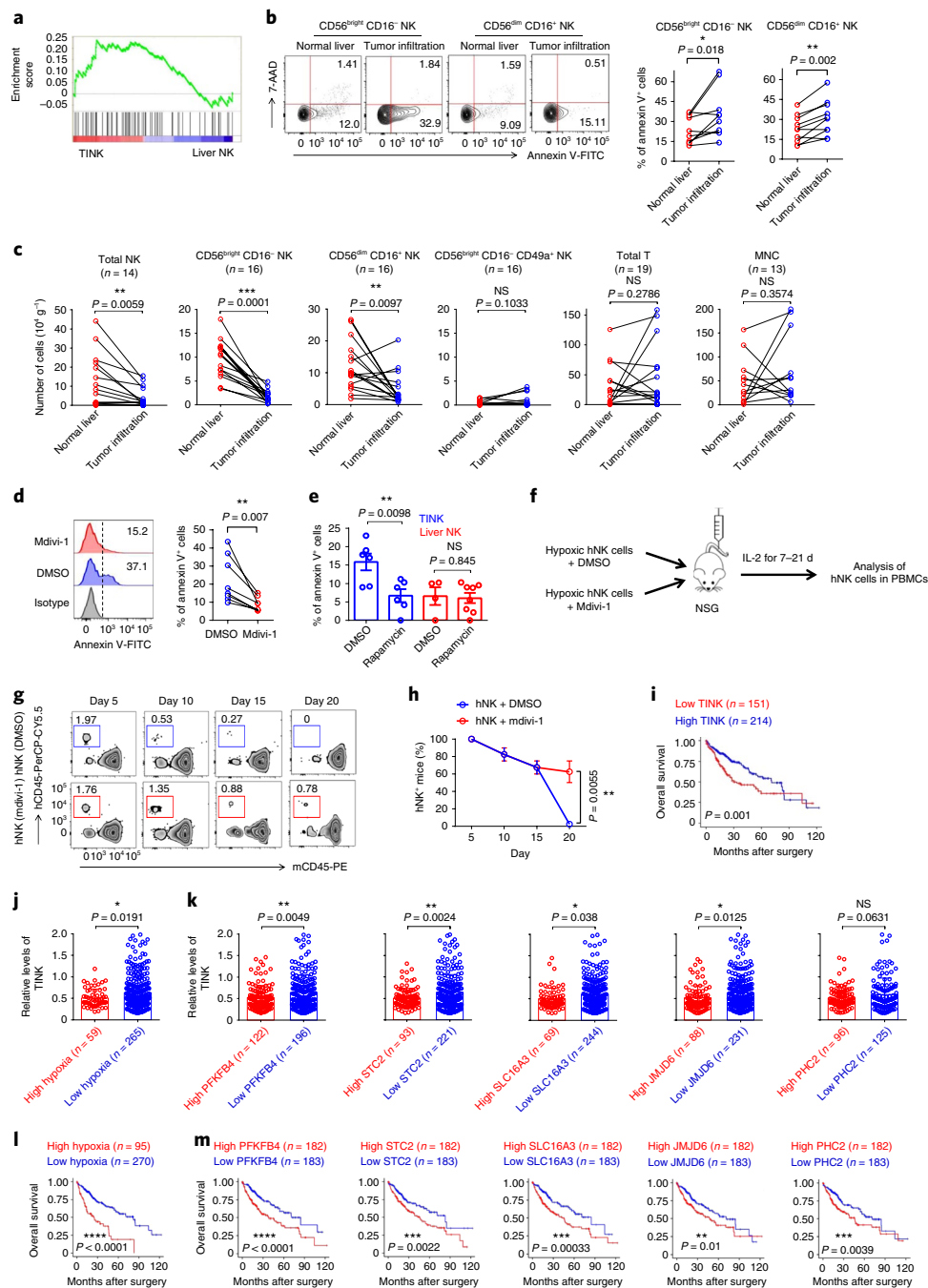


Fig. 4 | Mitochondrial fragmentation affects TINK cell survival. **a**, GSEA plots showing an increase in apoptosis signature (enrichment plot: HALLMARK_APOPTOSIS; Supplementary Table 4) in TINK cells ($n=2$) compared with normal liver NK cells ($n=2$). Data are representative of $n=4$ patients. **b**, Flow cytometry showing apoptosis (annexin V⁺) in CD56^{bright}CD16⁻ and CD56^{dim}CD16⁺ NK cells from tumor tissue or paired tumor-adjacent normal liver tissue from $n=10$ patients. Left: representative density plots of a sample. Middle and right: statistical calculation of all samples. **c**, Flow cytometry was used to analyze the numbers of NK cells (dead-CD45⁺CD56⁺CD3⁻), T cells (dead-CD45⁺CD56⁺CD3⁺) and MNCs in tumor tissue or paired tumor-adjacent normal liver tissue. **d,e**, Flow cytometry showing apoptosis (annexin V⁺) in TINK cells ($n=8$ patients) after treatment with mdivi-1 (**d**) or rapamycin (**e**). **d**, Left: representative MFI plot of a sample. Right: statistical calculation of all samples. **f-h**, Purified human peripheral NK cells were transferred into NOD SCID common gamma chain (NSG) mice via the tail vein. These NK cells were cultured under hypoxic conditions ($O_2 < 1\%$) and treated with mdivi-1 (10 nM) or DMSO (solvent control) for 3 d. **f** is a schematic of the procedure used. PBMC, peripheral blood mononuclear cell. **g**, The transferred hNK cells (hCD45⁺) in the peripheral blood MNC population of mice were tested on days 5, 10, 15 and 20 by flow cytometry. **h**, The proportion of hNK⁺ mice in each group is shown ($n=10$ per group). **i-m**, Analyses of $n=366$ biologically independent HCC samples from a TCGA dataset were performed. **i** shows a Kaplan-Meier analysis of overall survival in patients in the discovery cohort classified by their NK cell levels. Gene sets representing markers specific for NK cells are shown (Supplementary Table 4). **j,k**, Analyses of intratumoral NK cell levels in patients in the discovery cohort classified by their hypoxia grade (**j**; assessed via the expression of hypoxic gene signature sets) or expression of hypoxic signatures containing PFKFB4, STC2, SLC16A3, JMJD6 and PHC2 (**k**). **l,m**, Kaplan-Meier analyses of overall survival in patients in the discovery cohort classified by their hypoxia grade (**l**) and expression of hypoxia signatures containing PFKFB4, STC2, SLC16A3, JMJD6 and PHC2 (**m**). Data were analyzed by two-tailed paired Student's *t*-test (**b-d**), two-way ANOVA (**e**), two-tailed unpaired Student's *t*-test (**h,j,k**) or two-sided log-rank test (**i,l,m**). * $P < 0.05$; ** $P < 0.01$; *** $P < 0.005$; **** $P < 0.0001$. Data represent means \pm s.d.

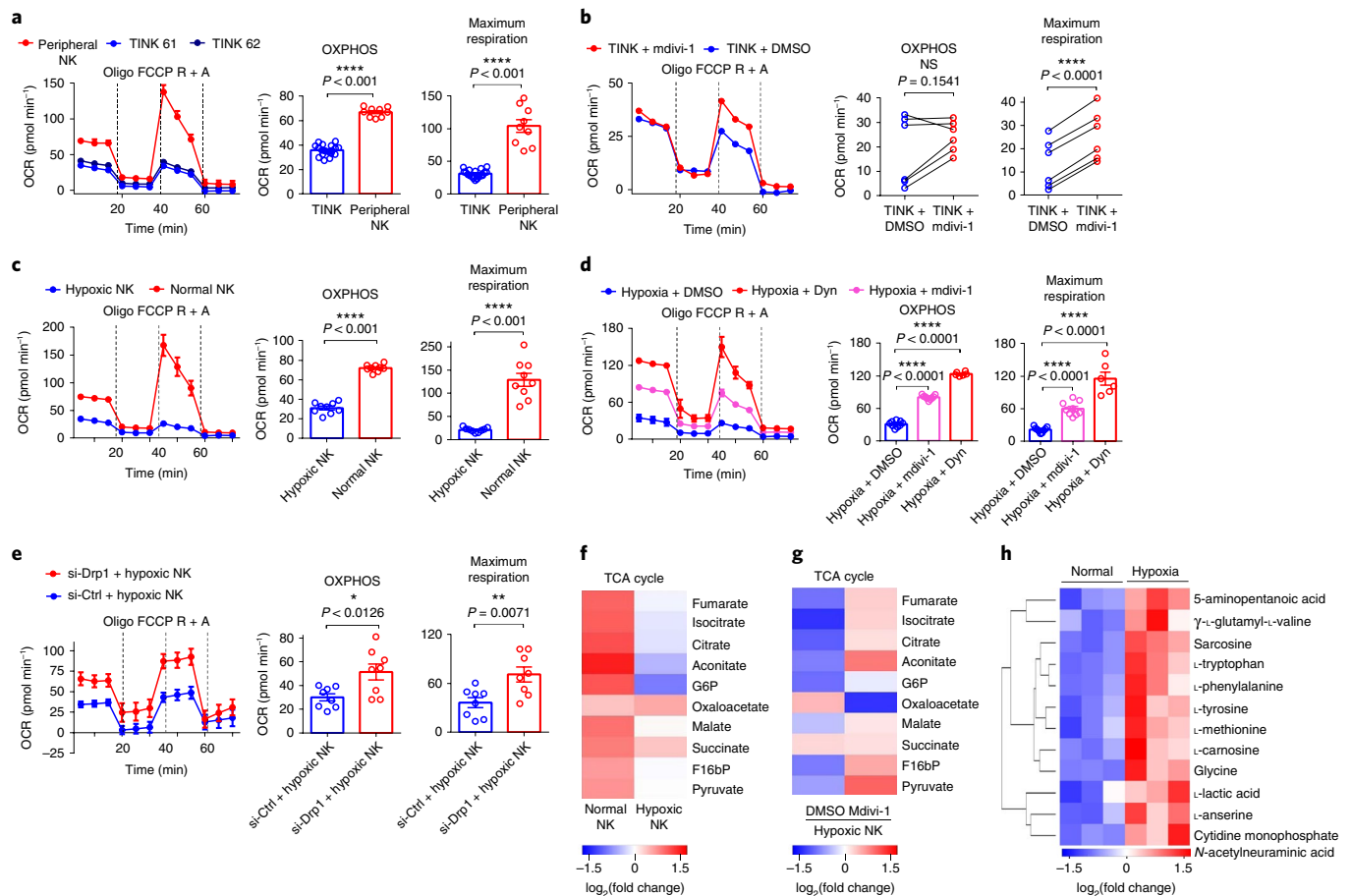


Fig. 5 | Aberrant mitochondrial metabolism is correlated with mitochondrial fragmentation in TINK cells. a–e, Left: the OCR of purified NK cells (purified using a MACS kit) was measured under basal conditions and in response to oligomycin (Oligo), the mitochondrial decoupler FCCP and rotenone + antimycin (R + A). Middle: basal OCR values (OXPHOS) were evaluated. Right: the maximum OCR values were those achieved after FCCP uncoupling (maximum respiration). **a**, OCR analyses of purified TINK cells ($n=18$ patients with liver cancer) and peripheral NK cells ($n=9$ donors) were performed. **b**, Purified TINK cells were pretreated with mdivi-1. The OCR was analyzed in $n=6$ patients per group. **c**, The OCRs of purified hypoxic- and normoxic-cultured peripheral NK cells ($n=9$ donors per group) are shown. **d**, Purified hypoxic-cultured peripheral NK cells pretreated with mdivi-1 (10 nM), Dyn (50 nM) or DMSO (solvent control) were evaluated. The OCR was analyzed for $n=9$ donors per group. **e**, The OCR of purified peripheral NK cells after hypoxic culture and knocking down Drp1 (si-Drp1) versus control cells (si-Ctrl) is shown for $n=8$ donors per group. **f–h**, Metabolomics analyses of intracellular metabolites of purified hypoxic- and normoxic-cultured peripheral NK cells treated with mdivi-1 (10 nM) or DMSO (solvent control) are shown. In **f** and **g**, heat maps show the normalized expression of TCA cycle components. **f**, Purified hypoxic- and normoxic-cultured peripheral NK cells are shown. **g**, Purified hypoxic-cultured peripheral NK cells pretreated with mdivi-1 (10 nM) or DMSO (solvent control). Each column depicts the mean of $n=3$ samples ($n=3$ per group). The heat map in **h** shows the upregulated expression of the metabolites of peripheral NK cells after hypoxic culture ($n=3$ per group). Data were analyzed by two-tailed unpaired Student's *t*-test. * $P < 0.05$; ** $P < 0.01$; **** $P < 0.0001$. Data are shown as means \pm s.d.

cells showed downregulation of the expression of the survival signal CD122 and upregulation of the expression of the exhaustion molecule T cell immunoglobulin and mucin-domain containing-3 (Supplementary Fig. 5g,h).

To test the correlation between mitochondrial fragmentation and apoptosis, we treated TINK cells with a low dose of mdivi-1 or rapamycin and found that these two inhibitors could reduce apoptosis in TINK cells (Fig. 4d,e). Furthermore, we established humanized NOD SCID common gamma chain mouse models via the transfer of human NK cells cultured under hypoxic conditions with or without pretreatment with mdivi-1 (Fig. 4f). IL-2 was injected into the recipient mice every 2 d to support NK cell survival in vivo. The inhibition of mitochondrial fragmentation by mdivi-1 increased the number of circulating NK cells and functional granzyme B expression in vivo (Fig. 4g,h and Supplementary Fig. 5i,j, right). We tested the mitochondrial phenotype of mdivi-1- and dimethyl sulfoxide (DMSO)-treated NK cells transferred in mice by MitoTracker Green and TMRM staining. Mdivi-1-pretreated

NK cells continued to show increased expression of TMRM and MitoTracker in vivo (Supplementary Fig. 5j, left and middle). Thus, mitochondrial fragmentation is correlated with TINK cell apoptosis and function.

To assess the relationship between NK cell loss and liver cancer progression, we analyzed the TCGA HCC dataset for NK cell abundance. Using specific gene sets for identifying NK cells³⁵ (Supplementary Table 4), we found that low intratumoral NK cell levels correlated with poor survival in patients with HCC (Fig. 4i). To confirm the impact of a hypoxic tumor microenvironment on intratumoral NK cell loss, we estimated the severity of tumor microenvironment hypoxia by generating hypoxic gene sets based on a hypoxic enrichment plot for the HCC dataset. We found that patients with severely hypoxic HCC possessed lower intratumoral NK cell levels than patients with less severely hypoxic HCC (Fig. 4j). Increased expression of the hypoxia markers *6-phosphofructo-2-kinase/fructose-2,6-bisphosphatase 4* (PFKFB4), *stanniocalcin 2* (STC2), *solute carrier family 16 member 3* (SLC16A3) or *jumonji domain*

containing 6 (*JMJD6*) predicted a reduced number of intratumoral NK cells in patients with HCC (Fig. 4k). Furthermore, analyses of overall survival using the Kaplan–Meier method revealed that having a severely hypoxic tumor microenvironment correlated with poor survival in patients with HCC, and that high expression of selected hypoxia markers predicted poor survival (Fig. 4l,m). Using an assay of antitumor-related immune-function molecules in a tumor microenvironment, we found that patients with severe hypoxia had lower intratumoral levels of granzyme A and granzyme K than patients with mild hypoxia (Supplementary Fig. 5k,l). Thus, NK cells have crucial roles in protection against liver cancer, and a hypoxic tumor microenvironment induces the loss of intratumoral NK cells. Taken together, these results suggested that a hypoxic tumor microenvironment correlates with mitochondrial fragmentation and the loss of antitumor NK cells.

Aberrant mitochondrial respiration is correlated with mitochondrial fragmentation in TINK cells. Fragmentation results in defective execution of mitochondrial functions and increased electron leakage during oxidative phosphorylation (OXPHOS)³⁶. We examined the metabolic output of TINK cells using a Seahorse XF Cell Mito Stress Test Kit. We found that the oxygen consumption rate (OCR), which is an indicator of OXPHOS, was lower in the TINK cells than in normal peripheral NK cells in the basal state (Fig. 5a). On injection of the mitochondrial decoupler carbonylcyano-4-(trifluoromethoxy)phenylhydrazone (FCCP), maximum respiration was reduced significantly in the TINK cells relative to the normal peripheral NK cells (Fig. 5a). To assess whether the restoration of mitochondrial morphology results in an increase in OXPHOS efficiency, we pretreated TINK cells with the fragmentation inhibitor mdivi-1. TINK cells treated in this manner did not show an increase in the basal OCR but, rather, an increase in the maximum OCR (Fig. 5b). Maximum respiration represents the maximum available mitochondrial capacity to generate sufficient energy under special conditions, and is considered to be important for the survival and function of cells³⁷. Consistent with the TINK cells, NK cells showed decreased basal and maximum respiration under hypoxic stress conditions (Fig. 5c). The inhibition of mitochondrial fragmentation by knocking down Drp1 expression and treating cells with mdivi-1 or Dyn enabled restoration of the rates of basal and maximum respiration in hypoxic NK cells (Fig. 5d,e). No changes in glycolytic signatures were observed between TINK cells and normal liver NK cells, and hypoxic stress induced a weak increase in the extracellular acidification rate (ECAR), which is

an indicator of glycolysis (Supplementary Fig. 6a,b). We wished to ensure that changes in the OCR were not due to the presence of NK cell subsets with different OCRs. Analyses of the OCRs of the two subsets of fresh peripheral NK cells ($CD56^{\text{bright}}CD16^-$ and $CD56^{\text{dim}}CD16^+$ cells) indicated that these two subsets exhibited similar mitochondrial respiration (Supplementary Fig. 6c). We analyzed the percentage of live purified TINK, peripheral NK and liver NK cells to exclude the effect of differences in cell viability on the OCR analysis (Supplementary Fig. 6d).

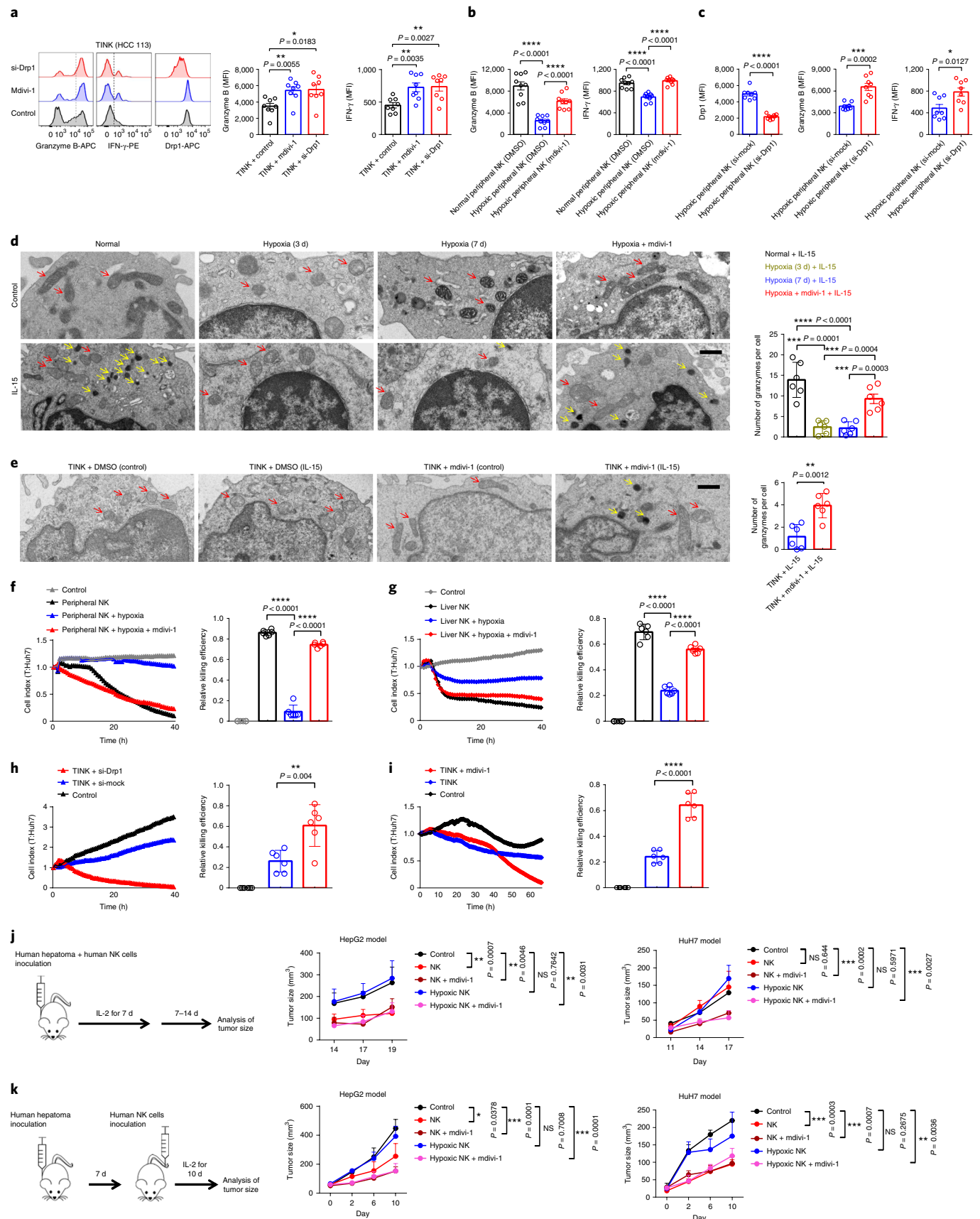
Next, unbiased metabolomics profiling of purified hypoxic- and normoxic-cultured NK cells revealed significant reductions in the expression of metabolic intermediates related to mitochondrial function, including the tricarboxylic acid (TCA) cycle, under the hypoxic stress conditions (Fig. 5f). Mdivi-1 treatment increased the expression of mitochondrial functional intermediates in the hypoxic-cultured NK cells, which indicated an increase in the rate of the TCA cycle (Fig. 5g). We found increased intracellular levels of various amino acids in the NK cells cultured under hypoxic conditions (Fig. 5h). Taken together, these results suggest that mitochondrial fragmentation is correlated with mitochondrial respiratory failure in TINK cells.

Restoration of mitochondrial morphology contributes to NK cell antitumor activity. Next, we investigated whether the restored mitochondrial structure correlated with the antitumor capacity of NK cells. We observed that TINK cells upregulated granzyme B and IFN- γ expression after knocking down Drp1 expression or pretreating the cells with mdivi-1 (Fig. 6a). Similar results were obtained in hypoxic-cultured NK cells after knocking down Drp1 and pretreating the cells with mdivi-1 (Fig. 6b,c). We measured the expression of intracellular granzyme in normoxic-cultured NK cells after IL-15 (50 ng ml⁻¹) stimulation (Fig. 6d). Granzyme expression was markedly reduced in hypoxic NK cells, but pretreatment with mdivi-1 could restore the cytoplasmic granzyme levels (Fig. 6d). TINK cells also showed impaired granzyme expression, but partial expression was restored following mdivi-1 pretreatment (Fig. 6e). In addition, we assessed the cytotoxic potential of NK cells with restored mitochondrial morphology by real-time cell index (xCELLigence) measurements. Pretreatment with mdivi-1 improved the ability of hypoxic-cultured peripheral NK cells and liver NK cells to induce significant cytotoxicity in human hepatoma cells (HuH7 cells) (Fig. 6f,g). The restoration of mitochondrial morphology by knocking down Drp1, and in response to mdivi-1 treatment, enabled TINK cells to kill tumor cells (Fig. 6h,i and Supplementary Fig. 6e).

Fig. 6 | Restoration of the mitochondrial metabolism of TINK cells contributes to an increased antitumor capacity. **a**, Flow cytometry analysis showing the expression of IFN- γ and granzyme B in TINK cells (dead- $CD45^+CD56^+CD3^-$) after knocking down Drp1 expression (si-Drp1) and treating the cells with mdivi-1 (10 nM). Left: representative MFI plots of a sample. Middle and right graphs show statistical calculation of granzyme B (middle) and IFN- γ (right) expression in all samples. **b,c**, Flow cytometry analysis showing the expression of IFN- γ (right) and granzyme B (left in **b**; middle in **c**) in hypoxic-cultured peripheral NK cells after knocking down Drp1 expression (si-Drp1) (**c**) and treating the cells with mdivi-1 (10 nM) (**b**). Drp1 knockdown efficiency plots are shown (left in **c**). Data are representative of $n=8$ patients per group in **a**, $n=9$ donors per group in **b** and $n=8$ donors per group in **c**. **d,e**, Left: TEM images showing intracellular granzyme and mitochondrial morphology in NK cells after IL-15 and IL-2 or control stimulation. Red arrows denote mitochondria, while yellow arrows denote granzymes. Scale bar, 1 μ m. **d**, Peripheral NK cells from normal donors ($n=6$) were cultured under hypoxic or normoxic conditions and pretreated with mdivi-1 (10 nM) or DMSO (solvent control). **e**, Purified TINK cells from patients with liver cancer ($n=6$) were pretreated with mdivi-1 (10 nM) or DMSO (solvent control). Right: numbers of granzyme molecules per cell (each dot represents the mean within a sample). **f-i**, Human HCC cells (HuH7) were used as targets in cytotoxicity assays with cultured NK cell effectors. Real-time cell index measurements (xCELLigence) of live target cells cultured with different effector NK cell ratios are shown (left). These are representative of the percentage of live target cells. The relative killing efficiency is also shown (right). No effector cells were included in the control group. **f,g**, Peripheral (**f**) and liver NK cells (**g**) were cultured under hypoxic conditions with mdivi-1 (10 nM) or DMSO. **h,i**, Purified TINK cells were evaluated after knocking down Drp1 expression (si-Drp1; **h**) and treating the cells with mdivi-1 (10 nM) or DMSO (**i**). $n=6$ per group in **f-i**. **j,k**, Mouse models of human HCC were established by subcutaneous injection of HepG2 or HuH7 cells. **j**, Peripheral NK cells from normal donors cultured under hypoxic or normoxic conditions with mdivi-1 or DMSO and HCC cells were injected subcutaneously into recipients. The procedure is outlined on the left. The tumor growth in HepG2 (middle) and HuH7 (right) mouse models of human HCC was assessed ($n=7$ mice per group). **k**, Peripheral NK cells from normal donors cultured under hypoxic or normoxic conditions with mdivi-1 or DMSO were transferred intravenously into recipients after 7 d of inoculation with the tumor ($n=8$ mice per group). Data were analyzed by two-way ANOVA (**a,b,d,f-k**) or two-tailed unpaired Student's *t*-test (**c,e**). * $P < 0.05$; ** $P < 0.01$; *** $P < 0.005$; **** $P < 0.0001$. Data represent means \pm s.d.

To ascertain whether the appropriate inhibition of mitochondrial fragmentation revised the killing capacity of tumor-localized NK cells *in vivo*, we co-injected (subcutaneously) human hepatoma

cells and purified human NK cells. IL-2 was injected into the recipient mice every 2d to support NK cell survival *in vivo*. Mdivi-1-pretreated hypoxic NK cells could control tumor growth,



but control-treated cells could not (Fig. 6j). We found that fewer hypoxic NK cells were distributed in the tumor compared with normal NK cells 10 d after transfer. Pretreatment with mdivi-1 increased the number of hypoxic NK cells in tumors (Supplementary Fig. 6f). Similar results were obtained in peritoneal hepatoma xenografts evaluated by D-luciferin-based bioluminescence (Supplementary Fig. 6g). mdivi-1 treatment strengthened rather than weakened the killing capability of normoxic NK cells (HuH7 model; Fig. 6j). Moreover, we investigated whether the revised mitochondrial morphology of circulating NK cells promotes antitumor functions in human hepatoma cells. We injected (subcutaneously) human hepatoma cells into recipient mice. Then, 7 d later, we adoptively transferred (intravenously) hypoxic NK cells that were supported in vivo by the injection of IL-2. Significantly smaller tumors were found in the mice reconstituted with the mdivi-1-treated normoxic or hypoxic NK cells than in the mice that received untreated hypoxia-cultured NK cells (Fig. 6k). Taken together, these data suggest that mitochondrial fragmentation is correlated with a decreased antitumor capacity in NK cells.

Discussion

Tumor-mediated immune evasion is targeted at different subsets of immune cells, and proceeds by numerous mechanisms (including the secretion of immunosuppressive factors and an imbalance in the inhibition and activation of receptors) that have been shown to contribute to tumor development^{38–41}. In the present study, in metabolic terms, mitochondrial fragmentation prevented NK cells from carrying out antitumor functions. Hypoxia was shown to be the crucial precipitating factor for mitochondrial fragmentation within NK cells. Therefore, hypoxia should be recognized as an immunosuppressive factor generated in tumors to drive immune escape. Taken together, our study results highlight a novel mechanism of immune escape for tumors, especially those associated with severe hypoxia.

The intricate tumor microenvironment is characterized by individuality, multiformity and heterogeneity. The causes of intratumoral immune cell dysfunction are dependent on the individual tumor microenvironment and tumor type. An earlier study focusing on lung cancer in mice, found that aberrant expression of fructose-1,6-bisphosphatase in NK cells inhibits glycolysis and leads to dysfunction dependent on transforming growth factor- β expression³⁹. Another study reported that glucose competition by tumor cells restricts the glycolytic capacity and IFN- γ production of T cells in a mouse sarcoma model⁶. Here, we demonstrated that a hypoxic tumor microenvironment induced excessive mitochondrial fission into fragments in NK cells, which contributed to immune escape in patients with liver cancer. In addition, we selected the hypoxia-related markers PFKFB4, STC2 and SLC16A3, which can predict low numbers of intratumoral NK cells, low levels of granzyme A and granzyme K, and poor survival in patients with HCC. We speculate that these markers could be used to predict intratumoral immune states.

mTOR is a key regulator of cellular metabolism and has fundamental roles in the immune response. We found that excessive activation of mTOR induced Drp1 phosphorylation, thereby resulting in mitochondrial fragmentation in NK cells. It has been reported that in NK cell-conditional knockout mice, constitutive mTOR activation causes a decrease in NK cell numbers, arrested development, exhaustive proliferation at an immature stage, and the loss of antitumor activities⁴². Enhancing autophagic activity by inhibiting mTOR promotes antigen-specific survival and memory formation in NK cells¹⁵. mTOR deficiency has a strong impact on the proliferation, maturation and activation of NK cells¹¹. An earlier study showed that an impaired mTOR pathway in obesity is responsible for the dysfunction of NK cells because it inhibits the formation of cytotoxic synapses⁴³. Thus, optimum mTOR activity is important for the

differentiation, survival and antitumor function of NK cells. Here, continuous hyperactivation of mTOR signaling due to the persistent stress of the hypoxic tumor microenvironment could be a key driver of exhaustion and the reduced antitumor capacity in NK cells.

The restoration of mitochondrial morphology by mdivi-1 treatment and Drp1 expression knockdown improved the antitumor capacity of NK cells in vitro and in vivo. Mdivi-1 is a widely used fission inhibitor that selectively targets Dyn and attenuates Drp1 self-assembly. Pretreatment with a suitable dose of mdivi-1 can aid cell survival by inhibiting the permeabilization of the mitochondrial outer membrane and reducing Bax/Bak-dependent mitochondrial release of cytochrome *c*⁴⁴. Some studies have shown the therapeutic potential of inhibitors of mitochondrial division in diseases with aberrant mitochondrial morphology²⁸. Thus, Drp1 inhibitors could have therapeutic application against tumors by restoring NK cells, but further study is required to ascertain the optimum dose and assess toxicity-induced tissue damage.

Online content

Any methods, additional references, Nature Research reporting summaries, source data, statements of code and data availability and associated accession codes are available at <https://doi.org/10.1038/s41590-019-0511-1>.

Received: 20 January 2019; Accepted: 4 September 2019;

Published online: 21 October 2019

References

- Barry, K. C. et al. A natural killer–dendritic cell axis defines checkpoint therapy-responsive tumor microenvironments. *Nat. Med.* **24**, 1178–1191 (2018).
- Lopez-Soto, A., Gonzalez, S., Smyth, M. J. & Galluzzi, L. Control of metastasis by NK cells. *Cancer Cell* **32**, 135–154 (2017).
- Morvan, M. G. & Lanier, L. L. NK cells and cancer: you can teach innate cells new tricks. *Nat. Rev. Cancer* **16**, 7–19 (2016).
- Dadi, S. et al. Cancer immunosurveillance by tissue-resident innate lymphoid cells and innate-like T cells. *Cell* **164**, 365–377 (2016).
- Ghesquiere, B., Wong, B. W., Kuchnio, A. & Carmeliet, P. Metabolism of stromal and immune cells in health and disease. *Nature* **511**, 167–176 (2014).
- Chang, C. H. et al. Metabolic competition in the tumor microenvironment is a driver of cancer progression. *Cell* **162**, 1229–1241 (2015).
- Gemta, L. F. et al. Impaired enolase 1 glycolytic activity restrains effector functions of tumor-infiltrating CD8⁺ T cells. *Sci. Immunol.* **4**, eaap9520 (2019).
- Ma, C. et al. NAFLD causes selective CD4⁺ T lymphocyte loss and promotes hepatocarcinogenesis. *Nature* **531**, 253–257 (2016).
- Sugiura, A. & Rathmell, J. C. Metabolic barriers to T cell function in tumors. *J. Immunol.* **200**, 400–407 (2018).
- Assmann, N. et al. Srebp-controlled glucose metabolism is essential for NK cell functional responses. *Nat. Immunol.* **18**, 1197–1206 (2017).
- Marçais, A. et al. The metabolic checkpoint kinase mTOR is essential for IL-15 signaling during the development and activation of NK cells. *Nat. Immunol.* **15**, 749–757 (2014).
- Keating, S. E. et al. Metabolic reprogramming supports IFN- γ production by CD56^{high} NK cells. *J. Immunol.* **196**, 2552–2560 (2016).
- Keppel, M. P., Saucier, N., Mah, A. Y., Vogel, T. P. & Cooper, M. A. Activation-specific metabolic requirements for NK cell IFN- γ production. *J. Immunol.* **194**, 1954–1962 (2015).
- O'Brien, K. L. & Finlay, D. K. Immunometabolism and natural killer cell responses. *Nat. Rev. Immunol.* **19**, 282–290 (2019).
- O'Sullivan, T. E., Johnson, L. R., Kang, H. H. & Sun, J. C. BNIP3- and BNIP3L-mediated mitophagy promotes the generation of natural killer cell memory. *Immunity* **43**, 331–342 (2015).
- Pearce, E. L., Poffenberger, M. C., Chang, C. H. & Jones, R. G. Fueling immunity: insights into metabolism and lymphocyte function. *Science* **342**, 1242454 (2013).
- Mills, E. L., Kelly, B. & O'Neill, L. A. J. Mitochondria are the powerhouses of immunity. *Nat. Immunol.* **18**, 488–498 (2017).
- Rambold, A. S. & Pearce, E. L. Mitochondrial dynamics at the interface of immune cell metabolism and function. *Trends Immunol.* **39**, 6–18 (2018).
- De Brito, O. M. & Scorrano, L. Mitofusin 2 tethers endoplasmic reticulum to mitochondria. *Nature* **456**, 605–610 (2008).

20. Cogliati, S. et al. Mitochondrial cristae shape determines respiratory chain supercomplexes assembly and respiratory efficiency. *Cell* **155**, 160–171 (2013).
21. Youle, R. J. & Karbowski, M. Mitochondrial fission in apoptosis. *Nat. Rev. Mol. Cell Biol.* **6**, 657–663 (2005).
22. Buck, M. D., O'Sullivan, D. & Pearce, E. L. T cell metabolism drives immunity. *J. Exp. Med.* **212**, 1345–1360 (2015).
23. Yu, T., Robotham, J. L. & Yoon, Y. Increased production of reactive oxygen species in hyperglycemic conditions requires dynamic change of mitochondrial morphology. *Proc. Natl Acad. Sci. USA* **103**, 2653–2658 (2006).
24. Vaupel, P. & Mayer, A. Hypoxia in tumors: pathogenesis-related classification, characterization of hypoxia subtypes, and associated biological and clinical implications. *Adv. Exp. Med. Biol.* **812**, 19–24 (2014).
25. Krzywinska, E. et al. Loss of HIF-1 α in natural killer cells inhibits tumour growth by stimulating non-productive angiogenesis. *Nat. Commun.* **8**, 1597 (2017).
26. Van der Bliek, A. M., Shen, Q. & Kawajiri, S. Mechanisms of mitochondrial fission and fusion. *Cold Spring Harb. Perspect. Biol.* **5**, a011072 (2013).
27. Taguchi, N., Ishihara, N., Jofuku, A., Oka, T. & Mihara, K. Mitotic phosphorylation of dynamin-related GTPase Drp1 participates in mitochondrial fission. *J. Biol. Chem.* **282**, 11521–11529 (2007).
28. Lackner, L. L. & Nunnari, J. Small molecule inhibitors of mitochondrial division: tools that translate basic biological research into medicine. *Chem. Biol.* **17**, 578–583 (2010).
29. Macia, E. et al. Dynasore, a cell-permeable inhibitor of dynamin. *Dev. Cell* **10**, 839–850 (2006).
30. Chen, H. et al. Mitofusins Mfn1 and Mfn2 coordinately regulate mitochondrial fusion and are essential for embryonic development. *J. Cell Biol.* **160**, 189–200 (2003).
31. Chen, H. & Chan, D. C. Emerging functions of mammalian mitochondrial fusion and fission. *Hum. Mol. Genet.* **14**, R283–R289 (2005).
32. Schofield, C. J. & Ratcliffe, P. J. Oxygen sensing by HIF hydroxylases. *Nat. Rev. Mol. Cell Biol.* **5**, 343–354 (2004).
33. Peng, H. et al. Liver-resident NK cells confer adaptive immunity in skin-contact inflammation. *J. Clin. Invest.* **123**, 1444–1456 (2013).
34. Bjorkstrom, N. K., Ljunggren, H. G. & Michaëlsson, J. Emerging insights into natural killer cells in human peripheral tissues. *Nat. Rev. Immunol.* **16**, 310–320 (2016).
35. Davoli, T., Uno, H., Wooten, E. C. & Elledge, S. J. Tumor aneuploidy correlates with markers of immune evasion and with reduced response to immunotherapy. *Science* **355**, eaaf8399 (2017).
36. Youle, R. J. & van der Bliek, A. M. Mitochondrial fission, fusion, and stress. *Science* **337**, 1062–1065 (2012).
37. Van der Windt, G. J. et al. Mitochondrial respiratory capacity is a critical regulator of CD8⁺ T cell memory development. *Immunity* **36**, 68–78 (2012).
38. Buck, M. D. et al. Mitochondrial dynamics controls T cell fate through metabolic programming. *Cell* **166**, 63–76 (2016).
39. Cong, J. et al. Dysfunction of natural killer cells by FBP1-induced inhibition of glycolysis during lung cancer progression. *Cell Metab.* **28**, 243–255 (2018).
40. Kaiser, B. K. et al. Disulphide-isomerase-enabled shedding of tumour-associated NKG2D ligands. *Nature* **447**, 482–486 (2007).
41. Kopp, H. G., Placke, T. & Salih, H. R. Platelet-derived transforming growth factor- β down-regulates NKG2D thereby inhibiting natural killer cell antitumor reactivity. *Cancer Res.* **69**, 7775–7783 (2009).
42. Yang, M. et al. NK cell development requires Tsc1-dependent negative regulation of IL-15-triggered mTORC1 activation. *Nat. Commun.* **7**, 12730 (2016).
43. Michelet, X. et al. Metabolic reprogramming of natural killer cells in obesity limits antitumor responses. *Nat. Immunol.* **19**, 1330–1340 (2018).
44. Cassidy-Stone, A. et al. Chemical inhibition of the mitochondrial division dynamin reveals its role in Bax/Bak-dependent mitochondrial outer membrane permeabilization. *Dev. Cell* **14**, 193–204 (2008).

Acknowledgements

We thank W. Tao for advice regarding RNA sequencing data analyses. This work was supported by the Natural Science Foundation of China (reference numbers 81330071, 81788101, 81872318 and 81602491) and the Strategic Priority Research Program of the Chinese Academy of Sciences (XDPB1002 and XDA12020217).

Author contributions

H.W., Z.T. and X.Z. conceived and conducted the project. H.W. supervised the project. X.Z. and H.W. wrote the paper. X.Z. performed the experiments and data analysis. D.J. contributed to the cell culture and mouse models. Y.Q., P.C., Y.S. and Y.J. collected tissue samples and information from patients. R.S. and B.F. contributed to the imaging analysis and interpreted the data. H.Z. performed the hypoxic experiments.

Competing interests

The authors declare no competing interests.

Additional information

Supplementary information is available for this paper at <https://doi.org/10.1038/s41590-019-0511-1>.

Correspondence and requests for materials should be addressed to Z.T. or H.W.

Peer review information Zoltan Fehervari was the primary editor on this article and managed its editorial process and peer review in collaboration with the rest of the editorial team.

Reprints and permissions information is available at www.nature.com/reprints.

Publisher's note Springer Nature remains neutral with regard to jurisdictional claims in published maps and institutional affiliations.

© The Author(s), under exclusive licence to Springer Nature America, Inc. 2019

Methods

Human samples. All human tissues used in the present study were obtained under the approval of the Ethics Committee of the University of Science and Technology of China (USTCEC201600004; Hefei, China). Written informed consent was obtained from all patients.

Fresh specimens from patients with liver cancer ($n = 116$) or benign disorders (calculus or hemangioma; $n = 26$) were collected from the First Affiliated Hospital of Anhui Medical University (Hefei, China). Patients were selected based on the primary disease and no treatment before resection. Pathology was based on cytological assessments and routine imaging. Tumor tissues, the junction of tumor and liver tissues, tumor-adjacent normal liver tissue and intraoperative peripheral blood were collected from patients with liver cancer. More normal liver tissues away from lesions were excised surgically from patients with benign hemangioma or calculus after ensuring they were not infected by hepatitis viruses or affected by cirrhosis (Supplementary Fig. 1a). Normal peripheral mononuclear cells (MNCs) were collected from 57 donors at the Blood Center of Anhui Province (Hefei, China). The clinical characteristics of all patients included in the present study are shown in Supplementary Tables 1–3.

Mice and cell lines. Female NOD-*Prkdc^{scid}* *IL2rg^{tm1}*/Bcgen (B-NOG; *Prkdc*^(-/-) and *IL2rg*^(X-/X-)) mice were purchased from Jianguo Biocytogen. All animals were kept in specific pathogen-free conditions. All experimental procedures involving mice were carried out as prescribed by the *National Guidelines for Animal Usage in Research* (China) and were approved by the Ethics Committee at the University of Science and Technology of China (reference: USTCACUC1701038).

The human liver cancer cells (HepG2 and HuH7) were purchased from the Shanghai Cell Bank (Chinese Academy of Sciences, Shanghai, China) and were verified by isoenzyme testing and DNA fingerprinting. All cell lines tested negative for *Mycoplasma*.

Isolation of human samples and NK cells. For the isolation of human samples, fresh tissues were washed with phosphate buffered saline (PBS), cut into small pieces and digested with collagenase type IV (1 mg ml⁻¹; Sigma–Aldrich) and DNase I (0.01 mg ml⁻¹; Sigma–Aldrich) in RPMI 1640 medium (Thermo Fisher Scientific) for 30 min at 37 °C. Then, lymphocytes were isolated with 30% Percoll density gradient and washed twice with PBS. Peripheral blood MNCs were isolated by Ficoll density gradients. NK cells were gated by dead⁻CD45⁺CD56⁺CD3⁻ and flow cytometry (Supplementary Fig. 1b). NK cells applied to microarray analyses (CD56^{bright}CD16⁻NK and CD56^{dimm}CD16⁺NK cells) were sorted by FACS Aria (BD Bioscience). NK cells applied to TEM, immunofluorescence assays and metabolic assays were purified by a magnetic-activated cell sorter (MACS) kit (Miltenyi Biotec). The purity of the NK cells was >93% for each assay (Supplementary Fig. 1c).

NK cell culture and treatment. NK cells were cultured in complete RPMI 1640 medium containing IL-2 (100 U ml⁻¹) and IL-15 (5 ng ml⁻¹; PeproTech). Hypoxic NK cells were kept in <1% O₂ balanced with N₂ in a Whitley H35 Hypoxystation (Don Whitley Scientific), whereas normoxic NK cells were cultured in 20% O₂ for 3–7 d. For experiments on hypoxic NK cells, vehicle control (DMSO), mdivi-1 (10 nM; Sigma–Aldrich), Dyn (25 nM; Sigma–Aldrich) or rapamycin (20 nM; Sigma–Aldrich) were added to cell supernatants at the initiation of hypoxic culture. For experiments on intratumoral NK cells, vehicle control (DMSO), mdivi-1 (10 nM) or rapamycin (20 nM) were added to the culture system for 24 h. In addition, freshly isolated TINKs were maintained in hypoxic culture for treatment for 24 h until analysis. NK cells were activated by culturing in complete RPMI 1640 medium containing IL-2 (100 U ml⁻¹) and IL-15 (20 ng ml⁻¹) under normoxic conditions for 24 h.

TEM. Purified NK cells were fixed with 2.5% glutaraldehyde at 4 °C for 12 h, then fixed in 2% osmium tetroxide. After adequate washing, samples were stained with 1% aqueous uranyl acetate. Samples were dehydrated with sequential washes in 50, 70, 90, 95 and 100% ethanol and immersed in Eponate 12 Resin. Samples were then cut into ultrathin sections and counterstained with uranyl acetate and lead citrate. Images were acquired with a transmission electron microscope (120 kV; Tecnai G2 Spirit; FEI). The long sides of mitochondria in each cell were analyzed using IMARIS 7.0 (Bitplane). The long side represents the length of a mitochondrion. The mean length of mitochondria in each sample was obtained by analyzing the length of each mitochondrion in a single cell and statistically analyzing 80–100 cells. NK cells were purified by a MACS kit (Miltenyi Biotec).

Flow cytometry. Cell suspensions were surface-labeled for human or mouse antibodies for 30 min at 4 °C. Homologous immunoglobulin G molecules were used as isotype control antibodies. Flow cytometry was carried out on a BD LSRII (Becton Dickinson) and analyzed by FlowJo. For intracellular staining, cells were fixed and permeabilized using a Foxp3/Transcription Factor Staining Buffer Set in accordance with the manufacturer's guidelines (eBioscience). Apoptosis was analyzed by Annexin V and 7-AAD double-staining according to the manufacturer's instructions (Becton Dickinson). All antibodies for flow cytometry staining are shown in Supplementary Table 5.

Immunofluorescence assays. For mitochondrial imaging, fresh isolated NK cells were stained with MitoTracker Green (catalog number M7514; Invitrogen) for 30 min, then fixed with 4% paraformaldehyde for nuclear staining. For co-imaging of mitochondrial and intracellular staining, cells were stained with MitoTracker Green, fixed (4% paraformaldehyde) and then permeabilized (0.1% Triton X-100; Shengong). Then, cells were incubated with primary antibodies and fluorescence-conjugated secondary antibodies and, finally, the nucleus was stained. We then carried out CLSM on an LSM 880 + Airyscan system (Zeiss). The antibodies used are shown in Supplementary Table 5. The long sides of mitochondria staining were analyzed using IMARIS 7.0 (Bitplane). The long side represents the relative length of a mitochondrion. The mean relative length of mitochondria in each sample was obtained by analyzing the length of each mitochondrion in a single cell and statistically analyzing 80–100 cells. The total intensity of Drp1^{ps616} represents the mean fluorescence intensity in a single cell. A total of 80–100 cells were collected for analysis in each sample. NK cells were purified using a MACS kit (Miltenyi Biotec).

Mitochondrial dynamic imaging. Human peripheral NK cells from healthy donors were purified using a MACS kit (Miltenyi Biotec). Purified human peripheral NK cells ($n = 8$ donors) were generated from hypoxic (O₂ < 1%) or normoxic cultures for 12 h. They were then used for 120 min of imaging. Mitochondria were stained with MitoTracker (green). We carried out live-cell imaging on an LSM 880 + Airyscan system (Zeiss). Definite Focus from Carl Zeiss is able to compensate for focal drift and can stabilize the sample in focus over long periods of time. Images were captured with a 63×/1.4-NA oil-immersion objective. Zeiss ZEN software (ZEN 2012; Carl Zeiss MicroImaging) was used to process the videos and images. During filming, NK cells were grown in a microscopy cell culture incubator and maintained under the previous hypoxic and normal oxygen conditions. We quantified mitochondrial fission events during 120 min of dynamic imaging. A mitochondrial fission into two is defined as a 'mitochondrial fission event'. Mitochondrial fission events in each cell were counted by observing 120 min of dynamic imaging. The frequency of mitochondrial fission events in each donor was obtained by measuring the frequency of mitochondrial fission events in a single cell and analyzing 30–40 cells statistically.

Small interfering RNA (siRNA) knockdown of Drp1 expression. NK cells were purified using a MACS (Miltenyi Biotec). siRNA-Drp1 (sc-43732; Santa Cruz Biotechnology) and siRNA-mock were transfected by electroporation into purified human peripheral NK cells and freshly isolated TINK cells using a Nucleofector Kit for Human Natural Killer Cells (VPA-1005; Lonza). Then, the transfected peripheral NK cells were cultured under hypoxic or normoxic systems and used for immunofluorescence assays. After electroporation, TINK cells were maintained in hypoxic culture for 24 h until analysis. We cultured TINK cells under hypoxia to maintain their already displayed state.

Immunoblotting. Fresh purified NK cells were lysed in RIPA buffer (Beyotime) containing 150 mM NaCl, 50 mM Tris (pH 7.4), 1% NP-40, 0.1% SDS, 0.5% sodium deoxycholate, EDTA, sodium orthovanadate, leupeptin sodium and fluoride. Cells were then lysed on ice for 30 min. The cell lysis solution was centrifuged at 12,000g for 10 min and supernatants collected. Samples were then run on precast 4–20% bis-tris protein gels (Genscript). Separated proteins were then transferred to PVDF membranes and blocked with 5% w/v milk overnight at 4 °C. Membranes were then incubated with primary antibodies in 5% w/v BSA in TBS containing 0.1% Tween-20 for 2 h at room temperature, then incubated with HRP-conjugated secondary antibodies (BOSTER) for 1 h at room temperature. Chemiluminescence autoradiography was used to develop protein bands. NK cells were purified using a MACS kit (Miltenyi Biotec).

Microarray analyses. Tissue NK cells and peripheral NK cells were purified by flow cytometry. NK cell purity was >94%, as confirmed by flow cytometry in post-isolation analyses. Cells were suspended in TRIzol Reagent (Invitrogen) and total RNA was extracted using an RNeasy Mini Kit (Qiagen). Before use, the RNA concentration was quantified using a NanoDrop 2000 spectrophotometer (Thermo Fisher Scientific) and RNA integrity was assessed using a bioanalyzer (2100; Agilent Technologies) and agarose gel electrophoresis. A human messenger RNA microarray system (4×44K; Agilent Technologies) was used to analyze 16 samples. All labeling and hybridization of samples was performed in accordance with the manufacturer's instructions. In brief, total RNA was reverse-transcribed into double-stranded complementary DNA, then transcribed into complementary RNA with labeled cyanine-3-CTP. Labeled complementary RNAs were then used for microarray hybridization. A scanner (G2505C; Agilent Technologies) was used to scan the microarrays. Raw data were extracted and analyzed by Feature Extraction version 10.7.1.1 (Agilent Technologies) and GeneSpring (Agilent Technologies). Raw data were normalized using a quantile algorithm. Differentially expressed genes were defined as a fold change ≥ 2.0 between the two groups and signal values beyond background signals. Afterwards, two online bioinformatics databases (Gene Ontology and the Kyoto Encyclopedia of Genes and Genomes) were applied to analyze the differentially expressed genes. Gene set enrichment analyses were performed to assess differences between TINK cells and normal

liver NK cells. Microarray data were deposited into the National Center for Biotechnology Information Gene Expression Omnibus repository (accession number: GSE120123).

Metabolomics assays. Purified hypoxic and normoxic NK cells treated with mdivi-1 (10 nM) or DMSO were washed with PBS and physiological (0.9%) saline. Cell pellets were reconstituted in 1 ml acetonitrile (ACN):MeOH:H₂O (2:2:1, v/v/v) (Sigma–Aldrich), sonicated for 10 min, incubated at –20 °C for 1 h, and centrifuged at 14,000g for 15 min at 4 °C. Supernatants were collected and evaporated to dryness in a vacuum concentrator for experimental analyses. For liquid chromatography–mass spectrometry, dry metabolites were reconstituted in 100 µl ACN:H₂O (1:1, v/v), centrifuged (15 min at 14,000g and 4 °C) to collect supernatants, and then transferred to high-performance liquid chromatography vials. Liquid chromatography–mass spectrometry was performed in multiple reaction monitoring (MRM) mode using an ultra-HPLC system (1290 Infinity LC; 1260 series for metabolic profiling; 1290 series for argininosuccinate and arginine tests; Agilent Technologies) and a mass spectrometer (5500 QTRAP; AB SCIEX). Samples (2 µl) were injected onto a Phenomenex Luna amino column (100 mm × 2.1 mm). For argininosuccinate and arginine tests only, samples (2 µl) were injected onto an ACQUITY UPLC BEH amino column (100 mm × 2.1 mm; Waters). Mobile phase A was an aqueous solution containing 25 mM ammonium hydroxide and 25 mM ammonium acetate. Mobile phase B was absolute ACN. The column was maintained at 25 °C and eluted at a flow rate of 300 µl min⁻¹. The linear gradient for elution was set from 85% mobile phase B and 15% mobile phase A to 100% mobile phase A in 10 min. Electrospray ionization source conditions were preset as follows: a temperature of 350 °C; a flow of 10–16 l min⁻¹; a capillary voltage of 4,000 V in positive mode and 3,500 V in negative mode; a nebulizer pressure of 30 psi and a nozzle voltage of 500 V. For target metabolites, MRM raw data were processed based on established metabolite MRM libraries and transition parameters.

Metabolic assays. For analyses of mitochondrial mass, fresh cells were stained with 100 nM MitoTracker Green in culture medium for 30 min at 37 °C. After washing twice with PBS, cells were surface-stained and processed for flow cytometry. For measurement of the mitochondrial membrane potential, fresh cells were stained with 100 nM TMRE in culture medium for 30 min at 37 °C. After washing twice with PBS, cells were loaded with surface markers and processed for flow cytometry. For measurement of mitochondrial superoxide production, fresh cells were incubated with 10 µM MitoSOX. After washing twice with PBS, cells were surface-stained and processed for flow cytometry. For measurement of the OCR and ECAR of NK cells, fresh isolated cells (200,000 cells well⁻¹) were plated on poly-l-lysine-pretreated Seahorse plates in XF media (25 mM glucose, 2 mM glutamine and 1 mM pyruvate) and analyzed using an XF-96 Extracellular Flux Analyzer (Agilent Technologies). Basal OCR and ECAR were measured for 30 min. Cells were treated with 2 mM oligomycin, 1.5 mM FCCP, and 1 mM each of rotenone and antimycin A (all drugs were from Agilent Technologies), to measure maximum respiration and excess respiratory capacity. The purity and viability of TINK, liver NK and peripheral NK cells were confirmed by flow cytometry in each post-isolation analysis. The purity (CD56⁺CD3⁻) and viability (7-AAD⁻) of NK cells were >93% for seahorse analysis (Supplementary Fig. 6d). NK cells were purified using the MACS kit. The subsets of NK cells (CD56^{bright}CD16⁻ and CD56^{dim}CD16⁺ NK cells) were sorted by FACS Aria.

Model of human liver cancer and NK cell transfer. Female B-NOG mice (6 weeks of age) were used to establish subcutaneous and peritoneal hepatoma xenografts to assess the antitumor capacity of mdivi-1-treated hypoxic NK cells. To assess the killing capacity of tumor-localized NK cells with a revised mitochondrial morphology, we injected (subcutaneously) human HepG2 or HuH7 cells (5 × 10⁶) into the axilla and, meanwhile, transferred normoxic or hypoxic NK cells (2 × 10⁶) with or without mdivi-1 pretreatment. IL-2 (75,000 U; Jiangsu Kingsley Pharmaceuticals) was injected (intraperitoneally) every 2 d to support NK cell survival in vivo. The tumor volume was calculated as (width² × length)/2. In addition, we established a peritoneal hepatoma xenograft by injecting (intraperitoneally) human HepG2-luciferase cells (5 × 10⁶) and, meanwhile, transferred hypoxic NK cells (2 × 10⁶) with or without mdivi-1 pretreatment. After 1 or 2 weeks, for tumor imaging in vivo, D-luciferin was injected (intraperitoneally) and imaged for 1 min using an IVIS Spectrum imaging system (Caliper Life Sciences). To assess the antitumor function of circulating NK cells with a revised mitochondrial morphology, we injected (subcutaneously) human HepG2 or HuH7 cells (5 × 10⁶) into the axilla to establish a subcutaneous xenograft model. After 1 week, we transfused 2 × 10⁶ normoxic or hypoxic NK cells with or without mdivi-1 pretreatment via the caudal vein, and injected (intraperitoneally) IL-2 (75,000 U) every 2 d to support NK cell survival in vivo. The tumor volume was calculated as (width² × length)/2. NK cells were purified using a MACS kit.

TCGA datasets assay. We analyzed 366 HCC samples and 49 normal liver tissue samples for hypoxic risk, point mutations, NK cell number and clinical parameters from a TCGA dataset (<https://tcga-data.nci.nih.gov>). The gene sets utilized for NK cell signatures and hypoxic signatures are presented in Supplementary Table 4.

A set of characteristic genes with expression specificity from the ImmGen database⁴⁵ was selected to define NK immune cells. To obtain NK gene sets, we identified gene sets as NK characteristic markers distinguishable from other immune cell types and combined the reported NK signatures³⁵. To estimate the numbers of intratumoral NK cells in different samples, the expression of the NK gene set (Supplementary Table 4) was determined by utilizing the fragments per kilobase of transcript per million mapped reads value of each gene after normalization to the mean and standard deviation among samples³⁵. One set of hypoxia-related genes from Kyoto Encyclopedia of Genes and Genomes enrichment (M19622: LEONARD_HYPOXIA) was selected to define the hypoxia scale. To obtain the grade of hypoxia in each sample, the expression of the gene set (Supplementary Table 4) was determined utilizing the fragments per kilobase of transcript per million mapped reads value of each gene after normalization to the mean and standard deviation among samples. For analyses of the mutation signature, we extracted valid data on somatic point mutations from the TCGA HCC dataset and analyzed them using MAF files. We defined a tumor sample as ‘mutated’ based on the predicted functional-related mutation containing nonsense mutations, frameshift mutations and missense mutations^{46,47}. The top-five high-frequency mutated genes (*TP53*, *CTNNB1*, *TTN*, *MUC16* and *ALB*) were screened. A one-sided Fisher’s exact test was utilized to estimate the correlation between mutation events and hypoxic features. For survival analyses, we utilized a univariate Cox proportional hazards model by glmnet (R)⁴⁸. X-tile plots were employed to assess the association between variables and survival by X-tile version 3.6.1 (Yale University School of Medicine). X-tile plots could select the best cut-off risk score automatically. Patients were classified into two groups based on whether the associated risk score was higher or lower than the cut-off risk score. The two groups were defined as ‘high risk’ or ‘low risk’, and Kaplan–Meier survival analyses and log-rank tests were performed. Analyses were carried out using R version 3.3.1.

Real-time cytotoxicity assays. The cytotoxicity assays of NK cells were monitored using an xCELLigence Real-Time Cell Analyzer–Multiple Plate system (Roche Applied Science). This platform measures unlinked adhesive target cells in real time. To obtain an equilibrium of E-Plate 16 (Roche Applied Science), we added 50 µl culture medium to each well. Human HCCs (HepG2 or HuH7; 1 × 10⁴ cells well⁻¹), as target cells in 100 µl culture medium, were seeded into E-Plate 16, which was then placed into the Real-Time Cell Analyzer–Multiple Plate instrument at 37 °C with 5% CO₂. After 24 h, NK cells (1 × 10⁵ cells well⁻¹), as effectors in 100 µl culture medium, were seeded into E-Plate 16 for killing. The cell index represented changes in electrical impedance, and reflected the number of unlinked target cells on biocompatible microelectrode surfaces. For real-time monitoring, the cell index was read automatically every 15 min. Cell index data in each group represented the mean value from three wells. NK cells were purified using a MACS kit.

Statistical analyses. Statistical significance was determined using Prism 6.0 (GraphPad version 6). Two-tailed unpaired or paired Student’s *t*-tests between two groups and two-way analysis of variance (ANOVA) across multiple groups were used to determine significance. The difference in overall survival was tested using log-rank tests. A one-sided Fisher’s exact test was utilized to estimate the correlation between mutation events and hypoxic features. Data represent means ± s.d. *P* < 0.05 was considered significant (**P* < 0.05; ***P* < 0.01; ****P* < 0.005; *****P* < 0.0001).

Reporting Summary. Further information on research design is available in the Nature Research Reporting Summary linked to this article.

Data availability

Microarray data were deposited into the National Center for Biotechnology Information Gene Expression Omnibus repository (accession number: GSE120123). The clinical characteristics of all patients included in the present study are shown in Supplementary Tables 1–3. All gene sets are shown in Supplementary Table 4. The antibodies used are shown in Supplementary Table 5. Full scans of all of the blots and gels are included in the Source Data. The data that support the findings of this study are available from the corresponding author upon request.

References

- Heng, T. S., Painter, M. W. & Immunological Genome Project Consortium. The Immunological Genome Project: networks of gene expression in immune cells. *Nat. Immunol.* **9**, 1091–1094 (2008).
- Adzhubei, I. A. et al. A method and server for predicting damaging missense mutations. *Nat. Methods* **7**, 248–249 (2010).
- Davoli, T. et al. Cumulative haploinsufficiency and triplosensitivity drive aneuploidy patterns and shape the cancer genome. *Cell* **155**, 948–962 (2013).
- Friedman, J., Hastie, T. & Tibshirani, R. Regularization paths for generalized linear models via coordinate descent. *J. Stat. Softw.* **33**, 1–22 (2010).

Reporting Summary

Nature Research wishes to improve the reproducibility of the work that we publish. This form provides structure for consistency and transparency in reporting. For further information on Nature Research policies, see [Authors & Referees](#) and the [Editorial Policy Checklist](#).

Statistics

For all statistical analyses, confirm that the following items are present in the figure legend, table legend, main text, or Methods section.

n/a Confirmed

- The exact sample size (n) for each experimental group/condition, given as a discrete number and unit of measurement
- A statement on whether measurements were taken from distinct samples or whether the same sample was measured repeatedly
- The statistical test(s) used AND whether they are one- or two-sided
Only common tests should be described solely by name; describe more complex techniques in the Methods section.
- A description of all covariates tested
- A description of any assumptions or corrections, such as tests of normality and adjustment for multiple comparisons
- A full description of the statistical parameters including central tendency (e.g. means) or other basic estimates (e.g. regression coefficient) AND variation (e.g. standard deviation) or associated estimates of uncertainty (e.g. confidence intervals)
- For null hypothesis testing, the test statistic (e.g. F , t , r) with confidence intervals, effect sizes, degrees of freedom and P value noted
Give P values as exact values whenever suitable.
- For Bayesian analysis, information on the choice of priors and Markov chain Monte Carlo settings
- For hierarchical and complex designs, identification of the appropriate level for tests and full reporting of outcomes
- Estimates of effect sizes (e.g. Cohen's d , Pearson's r), indicating how they were calculated

Our web collection on [statistics for biologists](#) contains articles on many of the points above.

Software and code

Policy information about [availability of computer code](#)

Data collection

The Flow cytometric data: LSR II and Aria II (BD Biosciences)
 The Mass Spectrometry data: 5500 QTRAP; AB SCIEX, Warrington, UK
 The Metabolic assays: XF-96 Extracellular Flux Analyzer (Agilent Technologies)
 The Real-time Cytotoxicity assays: xCELLigence Real-time Cell Analyzer (RTCA)-Multiple Plate (MP) system (Roche Applied Science)
 The Immunofluorescence assays: LSM 880+Airyscan system (Zeiss, Oberkochen, Germany)
 The Electron microscopy assays: Transmission electron microscope (120 kV; Tecnai™ G2 Spirit; FEI, Lausanne, Switzerland)

Data analysis

Statistical analysis: GraphPad Prism (ver. 6)
 Flow cytometric analysis: FlowJo (Version 7.6.1 for Windows)
 Real-time cytotoxicity analysis: xCELLigence experiment report (2.0.0.1301)
 Metabolic analysis: XF-96 Extracellular Flux Analyzer (Wave 2.2.0)
 Mass Spectrometry analysis: Analyst software (R)
 Microarray analyses: Feature Extraction v10.7.1.1 (Agilent Technologies) and GeneSpring (Agilent Technologies)
 Immunofluorescence analysis: ZEN 2012, IMARIS 7.0 (Bitplane, Geneva, Switzerland)
 The size of mitochondria analysis: IMARIS 7.0 (Bitplane, Geneva, Switzerland)
 Electron microscopy analysis: Serial EM 3.4.8

For manuscripts utilizing custom algorithms or software that are central to the research but not yet described in published literature, software must be made available to editors/reviewers. We strongly encourage code deposition in a community repository (e.g. GitHub). See the Nature Research [guidelines for submitting code & software](#) for further information.

Data

Policy information about [availability of data](#)

All manuscripts must include a [data availability statement](#). This statement should provide the following information, where applicable:

- Accession codes, unique identifiers, or web links for publicly available datasets
- A list of figures that have associated raw data
- A description of any restrictions on data availability

The main data that support the findings of this study are available in the article and its Supplementary Information. Microarray data were deposited into the National Center for Biotechnology Information GEO repository (accession number: GSE120123). Full scans of all the blots and gels were submitted as Source Data. The data that support the findings of this study are available from the corresponding author upon request.

Field-specific reporting

Please select the one below that is the best fit for your research. If you are not sure, read the appropriate sections before making your selection.

- Life sciences Behavioural & social sciences Ecological, evolutionary & environmental sciences

For a reference copy of the document with all sections, see [nature.com/documents/nr-reporting-summary-flat.pdf](https://www.nature.com/documents/nr-reporting-summary-flat.pdf)

Life sciences study design

All studies must disclose on these points even when the disclosure is negative.

Sample size	This sample size was sufficient to demonstrate statistically significant differences in comparisons between experimental groups by two-tailed Student t-test and ANOVA test. The sample size was also determined to be adequate based on the reproducibility between independent experiments.
Data exclusions	No data were excluded.
Replication	All experiments were either successfully replicated when using cell lines, or included a sufficient human sample size, taking into account the expected variability when using human samples and mice. Representative data was confirmed at least twice.
Randomization	Patients were selected based on the primary disease and no treatment before resection. Pathology was based on cytologic assessments and routine imaging. Health donors were randomly selected. Human samples and animals were randomly allocated to each group.
Blinding	Data collection of mouse tumor experiments were performed in a blinding manner. The investigators were not blinded in experiments with human tissues.

Reporting for specific materials, systems and methods

We require information from authors about some types of materials, experimental systems and methods used in many studies. Here, indicate whether each material, system or method listed is relevant to your study. If you are not sure if a list item applies to your research, read the appropriate section before selecting a response.

Materials & experimental systems

n/a	Involved in the study
<input type="checkbox"/>	<input checked="" type="checkbox"/> Antibodies
<input type="checkbox"/>	<input checked="" type="checkbox"/> Eukaryotic cell lines
<input checked="" type="checkbox"/>	<input type="checkbox"/> Palaeontology
<input type="checkbox"/>	<input checked="" type="checkbox"/> Animals and other organisms
<input type="checkbox"/>	<input checked="" type="checkbox"/> Human research participants
<input checked="" type="checkbox"/>	<input type="checkbox"/> Clinical data

Methods

n/a	Involved in the study
<input checked="" type="checkbox"/>	<input type="checkbox"/> ChIP-seq
<input type="checkbox"/>	<input checked="" type="checkbox"/> Flow cytometry
<input checked="" type="checkbox"/>	<input type="checkbox"/> MRI-based neuroimaging

Antibodies

Antibodies used

Anti-human CD56 PE-CY7, BD Pharmingen, Cat#557747, Lot#8242831, Clone#B159, 2µl per test;
 Anti-human CD3 APC-CY7, Biolegend, Cat#300318, Lot#B268668, Clone#HIT3a, 2µl per test;
 Anti-human CD45 PerCP-CY5.5, Biolegend, Cat#368504, Lot#B266809, Clone#2D1, 2µl per test;
 Anti-human CD16 PerCP-CY5.5, Biolegend, Cat#302028, Lot#B21187, Clone#3G8, 2µl per test;
 Anti-human CD16 FITC, BD Pharmingen, Cat#555406, Lot#6263705, Clone#3G8, 2µl per test;
 Anti-human CD49a PE, BD Pharmingen, Cat#559596, Lot#5274538, Clone#SR84, 2µl per test;
 Anti-human CD56 PE, BD Pharmingen, Cat#555516, Lot#5114914, Clone#B159, 2µl per test;
 Anti-human CD11b Alexa-488, BD Pharmingen, Cat#557701, Lot#4304527, Clone#ICRF44, 2µl per test;

Anti-human CD27 FITC, BD Pharmingen, Cat#555440, Lot#8151611, Clone#M-T271, 2µl per test;
 Anti-human CD122 PE, BD Pharmingen, Cat#554525, Lot#5138596, Clone#Mik-β3, 2µl per test;
 Anti-human Tim3 PE, R&D, Cat#555967, Lot#YGR0714011, Clone#344823, 2µl per test;
 Anti-human CTLA-4 PE, BD Pharmingen, Cat#555700, Lot#5351582, Clone#BNi3, 2µl per test;
 Anti-human NKG2A PE, R&D, Cat#FAB138P, Lot#LA0913111, Clone #131411, 2µl per test;
 Anti-human CD103 FITC, BD Pharmingen, Cat#550259, Lot#7180763, Clone #Ber-ACT8, 2µl per test;
 Anti-human CD69 PE, BD Pharmingen, Cat#555531, Lot#5204788, Clone #FN50, 2µl per test;
 Anti-human NKP46 PE, BD Pharmingen, Cat#558563, Lot#2300905, Clone #9E2/NKp46, 2µl per test;
 Anti-human CD127 FITC, BD Pharmingen, Cat#560549, Lot#3046698, Clone #HIL-7R-M21, 2µl per test;
 Anti-human Granzyme B Alexa-647, Biolegend, Cat#372219, Lot#B233111, Clone #QA16A02, 2µl per test;
 Anti-human CD107a APC, BD Pharmingen, Cat#560664, Lot#7082937, Clone #H4A3, 2µl per test;
 Anti-human IFN-γ PE, BD Pharmingen, Cat#559327, Lot#5057550, Clone #B27, 2µl per test;
 Anti-human TNF-α PE, R&D, Cat#FAB2463P, Lot#4307714, Clone #6402, 2µl per test;
 Anti-human Drp-1, Abcam, Cat#ab184247, 2µl per test;
 Anti-human Phospho-DRP1 (Ser616), Cell signaling technology, Cat# 3455S, Lot#5, 1:1000;
 Anti-human Phospho-S6 Ribosomal Protein PE, Cell signaling technology, Cat#5316S, Lot#7, 2µl per test;
 Anti-human mTOR (pS2448) PE, BD Pharmingen, Cat#563489, Lot#6231762, Clone #O21-404, 2µl per test;
 Anti-human P-4EBP1 Alexa Fluor 488, BD Pharmingen, Cat#560287, Lot#7132707, Clone #M31-16, 2µl per test;
 Anti-human Ki-67 Alexa-488, Biolegend, Cat#151204, Lot#B235021, Clone #16A8, 2µl per test;
 Anti-Mouse IgG1, κ FITC, BD Pharmingen, Cat#555748, Lot#6301865, Clone #MOPC-21, 2µl per test;
 Anti-Mouse IgG2a, κ FITC, BD Pharmingen, Cat#555573, Lot#2664, Clone #G155-178, 2µl per test;
 Anti-Mouse IgG1, κ Alexa-488, BD Pharmingen, Cat#557702, Lot#3053827, Clone #MOPC-21, 2µl per test;
 Anti-Mouse IgG1, κ Alexa-647, BD Pharmingen, Cat#557714, Lot#7187734, Clone #MOPC-21, 2µl per test;
 Anti-Rat IgG2a, κ PE-CY7, BD Pharmingen, Cat#552784, Lot#6126853, Clone #R35-95, 2µl per test;
 Anti-MTP18 Antibody, Abcam, Cat#ab198217, 1:500;
 Anti-DRP1(Phospho-S637) Antibody, Sigma, Cat#SAB4301399, Lot#461211842, 1:500;
 Anti-Phospho-p70 S6 Kinase Antibody, Cell signaling technology, Cat#9204, Lot#2, 1:1000;
 Anti-HIF-1α Antibody, Cell signaling technology, Cat#36169, Lot#1, Clone #D1S7W, 2µl per test;
 Anti-Drp1 Antibody, Cell signaling technology, Cat#8570, Lot#3, Clone #D6C7, 1:1000;
 Anti-Mitofusin-1 Antibody, Cell signaling technology, Cat#14739, Lot#1, Clone #D6E2S, 1:1000;
 Anti-Mitofusion-2 Antibody, Cell signaling technology, Cat#11925, Lot#1, Clone #D1E9, 1:1000;
 Anti-Opa1 Antibody, Cell signaling technology, Cat#67589, Lot#1, Clone #D7C1A, 1:1000;
 Anti-AKT Antibody, Proteintech, Cat#10176-2-AP, 1:1000;
 Anti-Phospho-AKT Antibody (Ser473) BV421, BD Pharmingen, Cat#562599, Lot#6245614, Clone #M89-61, 2µl per test;
 Anti-Phospho-AKT Antibody (Ser473), Cell signaling technology, Cat#4058s, Lot#1, 1:1000.

Validation

All antibodies used in this study were validated for species and application by the vendors, and were cited by other publications. All antibodies were validated and titrated using isotype or biological control. We further validated the primary antibodies used in blots by their molecular weight.

Eukaryotic cell lines

Policy information about cell lines

Cell line source(s)	The human liver-cancer cells HepG2 and HuH7 were purchased from the Shanghai Cell Bank (Chinese Academy of Sciences, Shanghai, China).
Authentication	Cells were appraised by an isoenzymes test and DNA-fingerprinting by Shanghai Cell Bank (Chinese Academy of Sciences, Shanghai, China).
Mycoplasma contamination	All cell lines were tested negative for mycoplasma contamination.
Commonly misidentified lines (See ICLAC register)	No commonly misidentified cell lines were used.

Animals and other organisms

Policy information about studies involving animals; ARRIVE guidelines recommended for reporting animal research

Laboratory animals	Female NOD-Prkdcscid IL2rgtm1/Bcgen (B-NOG; Prkdc (-/-), IL2rg (X-/X-)) mice (6w) were purchased from Jiangsu Biocytogen (Jiangsu, China).
Wild animals	The study did not involve wild animals.
Field-collected samples	The study did not involve samples collected from the field.
Ethics oversight	All experimental procedures involving mice were carried out as prescribed by the National Guidelines for Animal Usage in Research (China) and were obtained by approval of the Ethics Committee at the University of Science & Technology of China (USTCACUC1701038).

Note that full information on the approval of the study protocol must also be provided in the manuscript.

Human research participants

Policy information about [studies involving human research participants](#)

Population characteristics	Normal peripheral mononuclear cells were collected from 57 donors at the Blood Center of Anhui Province (Hefei, Anhui, China). Fresh specimens from patients with liver cancer or benign (calculus or hemangioma) disorders were collected from the First Affiliated Hospital of Anhui Medical University (Hefei, Anhui, China). Patients were selected based on the primary disease and no treatment before resection. Pathology was based on cytologic assessments and routine imaging. We collected 116 samples of liver cancer, including 95 males and 21 females, with an average age of 57 years. We collected 26 samples of benign liver diseases, including 3 males and 23 females, with an average age of 49.6 years. Clinical characteristics of all patients in the present study are shown in Supplementary Table 1–3.
Recruitment	Samples were obtained from the in-patient department of the First Affiliated Hospital of Anhui Medical University (Hefei, Anhui, China). Potential participants were screened based on their clinical diagnosis. The participants were voluntary. There is no self-selection bias.
Ethics oversight	All human tissues used in the present study were obtained under approval of the Ethics Committee of the University of Science & Technology of China (USTCEC201600004; Hefei, China). Written informed consent was obtained from all patients.

Note that full information on the approval of the study protocol must also be provided in the manuscript.

Flow Cytometry

Plots

Confirm that:

- The axis labels state the marker and fluorochrome used (e.g. CD4-FITC).
- The axis scales are clearly visible. Include numbers along axes only for bottom left plot of group (a 'group' is an analysis of identical markers).
- All plots are contour plots with outliers or pseudocolor plots.
- A numerical value for number of cells or percentage (with statistics) is provided.

Methodology

Sample preparation	NK cells were purified by a magnetic-activated cell sorter (MACS) kit (Miltenyi Biotec, Cologne, Germany) or sorting by FACS Aria II (BD Bioscience, San Jose, CA, USA). Isolation of human samples and NK cells were described in Methods. NK cells were maintained cultured in complete RPMI 1640 medium containing IL-2 (100 U/mL) and IL-15 (5 ng/mL). Detail of NK cell culture was described in Methods.
Instrument	The Flow cytometric data were collected by LSR II and Aria II (BD Biosciences).
Software	Data were analysed with FlowJo (Version 7.6.1 for Windows).
Cell population abundance	NK cells were purified by a MACS kit or FACS Aria. The purity was higher than 93% as determined by secondary flow-cytometric analysis (as shown in Supplementary Figure 1c).
Gating strategy	For all experiments, cells were first gated by FSC/SSC to exclude debris, followed by gating FSC-A and FSC-H to eliminate non-singlets. Then, target cell population for further analysis were gated by cell surface marker. NK cells were gated by dead- CD45 +CD56+CD3- (as shown in Supplementary Figure 1b).

- Tick this box to confirm that a figure exemplifying the gating strategy is provided in the Supplementary Information.